

Nitrate promoted ATZ degradation in Z-scheme $\text{Cs}_3\text{Bi}_2\text{I}_9/\text{BiVO}_4$ photocatalytic system: Coupling $\cdot\text{OH}$ and RNS mediated reduction and oxidation

Xinyu Duan ^a, Huiping Jia ^a, Tingting Cao ^{a,b}, Hongbin Yu ^{a,b}, Yanan Zhang ^a, Ying Lu ^{a,b,*}, Dandan Zhou ^{a,b}

^a Engineering Lab for Water Pollution Control and Resources Recovery, School of Environment, Northeast Normal University, Changchun 130117, China

^b Engineering Research Center of Low-Carbon Treatment and Green Development of Polluted Water in Northeast China, Ministry of Education, Northeast Normal University, Changchun 130117, China



ARTICLE INFO

Keywords:

Nitrate
Reactive nitrogen species
ATZ
 $\text{Cs}_3\text{Bi}_2\text{I}_9/\text{BiVO}_4$
 $\cdot\text{OH}$

ABSTRACT

Nitrate, widely present in water, can be excited by UV light and generate reactive nitrogen species (RNS) etc., facilitating pollutants selective degradation. In this work, the promoting effect of nitrate on atrazine removal in the Z-scheme $\text{Cs}_3\text{Bi}_2\text{I}_9/\text{BiVO}_4$ (CBI/BVO) photocatalytic system was studied. The CBI/BVO composite utilized CBI and BVO excitation to enhance photogenerated carriers production, and the Z-scheme heterojunction to increase photoinduced carriers separation yield, with a maximum value of 15.41 times that of pure BVO, releasing CBI electrons and BVO holes with powerful redox ability. Thanks to nitrate addition, the atrazine degradation improved, whose kinetic constant was 14.46 and 2.37 times higher than that of nitrate photolysis and 0.32-CBI/BVO photocatalysis. DFT, HPLC-MS, EPR, and toxicity assessments indicated the electron rich portion of atrazine and its intermediates were susceptible to RNS attack and underwent dechlorination, that combined with the oxidation brought by $\cdot\text{OH}$, synergistically promoting atrazine degradation, mineralization, and detoxification.

1. Introduction

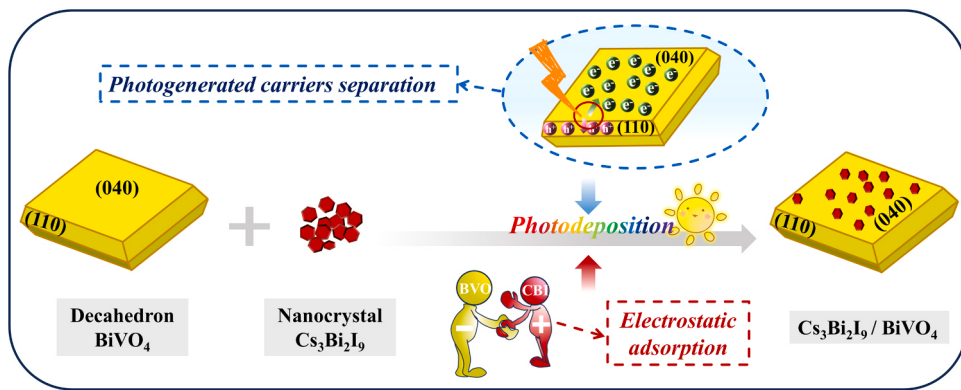
Due to the broad-spectrum, high efficiency, and low price, atrazine (ATZ) has been used in over 80 countries including China and United States for over 40 years, being one of the most popular herbicides in the world [1]. The characteristics of easy residue, high mobility, and long half-life make it the most common pollutant, and high concentrations of ATZ residues (0.67–1289.5 $\mu\text{g/L}$) have been detected in the surface and groundwater of many countries and regions [2,3]. This distribution situation is particularly worrying as ATZ can disrupt cell chromosome structure and estrogen metabolism, posing threat to human health and ecological safety [4,5]. Traditional wastewater treatment methods including adsorption, biodegradation, and membrane technology, etc. are limited by the issues such as low efficiency, high cost, long cycle time, and secondary pollution in ATZ pollution elimination [6–8]. Therefore, developing novel remediation technologies is great urgent.

Solar-driven semiconductor photocatalysis has attracted widespread attention because of its high efficiency, environmentally friendly, strong

adaptability, and low secondary pollutants [9]. Under irradiation, reactive oxygen species (ROS) such as $\cdot\text{OH}$ and $\cdot\text{O}_2^-$ are in situ generated at the catalyst surface or in bulk phase, and then react with pollutants at high rate constants ($>10^9 \text{ /M s}$) via electron transfer, H extraction, or free radical addition [10]. Due to the rich in saturated hydrocarbon groups with high electrical density, ATZ is prone to be attacked by $\cdot\text{OH}$ which exhibits strong electrophilic properties, causing the detachment of chemical groups such as ethylamino and isopropyl groups and the consequent mineralization [11]. Electronic band structure engineering, surface vacancy strategy and ion doping are utilized to regulate and control the generation, separation and transport of photogenerated carriers within photocatalyst, so as to strengthen the pollutants degradation and detoxification, which is currently the focus and difficulty of photocatalytic removal of ATZ [12–14]. BiVO_4 (abbreviated as BVO) is a direct bandgap semiconductor with narrow bandgap ($\sim 2.4 \text{ eV}$) that can respond to visible light, as well as the suitable valence band ($\sim 2.8 \text{ eV}$) which endows photogenerated holes with strong oxidation capability [15–17]. Among them, monoclinic BVO could achieve the directional

* Corresponding author at: Engineering Lab for Water Pollution Control and Resources Recovery, School of Environment, Northeast Normal University, Changchun 130117, China.

E-mail address: luy332@nenu.edu.cn (Y. Lu).



Scheme 1. Schematic diagram of CBI/BVO preparation process.

transfer of photogenerated electrons and holes towards (040) and (110) crystal planes due to its valence band and conduction band energy difference between crystal planes, exhibiting intensified carrier separation [18–20]. $\text{Cs}_3\text{Bi}_2\text{I}_9$ (abbreviated as CBI) is a low toxic and stable halogen perovskite, which has good visible light harvesting and strong reduction ability caused by its narrow bandgap (~ 1.9 eV) and relatively negative conduction band (~ -1.1 eV), becoming a potential photocatalyst for contaminates decomposition [21–23]. Because of safety, non-toxic, cheap and easy to obtain, these Bi-based catalysts have already been served as "green materials" and used widely in medicine, catalyst, battery and other fields [24,25]. However, both BVO and CBI are restricted by their rapid charge recombination. Z-scheme heterojunction can drive the photogenerated charge carriers transfer through a built-in electric field, improving the quantum yield, meanwhile, maximally maintain the electrons and holes with powerful redox ability, promoting pollutants efficient removal [22,24].

Nitrogen is an essential nutrient and important component of living organisms [26]. However, excessive nitrogen utilization could contaminate surface water which is the main source of drinking water, especially in areas with intensive agricultural activities, making nitrate one of the most abundant and widespread environmental pollutants [27]. Photocatalytic reduction of nitrate is considered to be a promising pollution control technology. The photoinduced electrons efficiently reduce nitrate to harmless nitrogen, while for holes generated synchronously with electrons, some organic matters such as formic acid may be added as electron donors, forming the redox reactions cycle [28, 29]. However, the addition of these chemicals could bring secondary pollution, elevated cost and complex operation. The electron-donated moieties in ATZ enable it to serve as a natural and efficient hole sacrificial agent, promoting the nitrate reduction [30]. Although ATZ and nitrate are often simultaneously monitored in agricultural runoff [31–33], there are few studies about their coexisting removal.

Notably, under irradiation of UV light with wavelength greater than 200 nm, nitrate can be excited and produce powerful reactive nitrogen species (RNS, like $\cdot\text{NO}_2$ and $\cdot\text{NO}$) as well as reactive oxygen species (ROS, like $\cdot\text{OH}$ and $\text{ROO}\cdot$) [34–37]. Compared with h^+ and $\cdot\text{OH}$, the oxidation ability of RNS is relatively weak, for instance the oxidation potential of $\cdot\text{NO}_3$, $\cdot\text{NO}_2$ and $\cdot\text{NO}$ are 2.30, 1.03 and 0.39 V, respectively [37]. However, they can accelerate electron-rich pollutants decomposition through electron transfer, forming a complementary pathway with $\cdot\text{OH}$ which degrades pollutants via hydrogen transfer and addition [38]. Thus, the photolysis of nitrates, which acted as a common background component of ground, surface, and wastewater matrix, could exert a significant impact on the fate of co-existed contaminates. Some results indicate that the $\cdot\text{HO}$ and RNS generated from nitrate photolysis can efficiently degrade thiamphenicol, enrofloxacin, tetracycline etc. [39–41]. However, the formed nitrate transformation products are sometimes more toxic and persistent than their parent compounds, such as the nitrophenol and nitrophenol produced in nitrate-induced phenol

photolysis, hindering the development of nitrate-sensitized pollutant degradation [42]. Although some researches have been conducted on the photochemical behavior of ATZ in the presence of nitrate, as well as the photocatalytic degradation of ATZ and nitrate, respectively, there is little study on the removal effect and enhancement mechanism of nitrate on ATZ in photocatalytic systems.

In this work, the promoting effect of nitrate on ATZ degradation in the Z-scheme CBI/BVO photocatalytic system were systematically investigated. The simultaneous excitation of CBI and BVO improves the light harvesting efficiency and thus increases the quantity of photogenerated charge carriers. The Z-scheme heterojunction not only intensifies the yield of photogenerated carrier separation, but also preserves the high conduction band of CBI and the valence band of BVO. The releasing electrons on CBI reduce nitrate to nitrogen, as well as the BVO holes are consumed by ATZ containing electron donating groups, meanwhile, the RNS produced by nitrate photolysis accelerate the mineralization and detoxification of ATZ, ultimately achieving synchronous and synergistic removal of two pollutants. The synergistic catalytic mechanisms were specifically explored via radicals quenching experiments, electron paramagnetic resonance spectroscopy, intermediate products identification, and density functional theory calculation. This work emphasizes the importance of reduction and oxidation mediated by $\cdot\text{OH}$ and RNS in the efficient removal of ATZ, and provides a new approach for repairing water contaminated by nitrate and organic pollutants.

2. Experimental

2.1. Materials

Cesium iodide (CsI), bismuth iodide (BiI_3), and bismuth nitrate pentahydrate ($\text{Bi}(\text{NO}_3)_3 \cdot 5 \text{ H}_2\text{O}$) were purchased from Ron Chemical Reagent. Ammonium vanadate (NH_4VO_3) and potassium nitrate (KNO_3) were provided by Tianjin Damao Chemical Reagent Co., Ltd. ATZ ($\text{C}_8\text{H}_{14}\text{ClN}_5$), nitric acid (HNO_3), ammonia water ($\text{NH}_3 \cdot \text{H}_2\text{O}$), and N, N-dimethylformamide (DMF) were obtained from Aladdin Reagent (Shanghai) Co., Ltd. The above reagents have not been secondary treated, and the water used was high purity deionized water.

2.2. Catalyst preparation

Preparation of $\text{Cs}_3\text{Bi}_2\text{I}_9$ (CBI): 0.18 mM CsI and 0.12 mM BiI_3 were first dissolved into 1.5 mL DMF. After magnetically stirring until transparent, 50 μL oleamine and 0.3 mL oleic acid were dropped into aforementioned solution. Then the mixture was dispersed into 20 mL toluene, magnetically stirred for 5 min, centrifuged for 3 min at 5000 r/min to get the low-layered precipitate. After washing with toluene, centrifuged at 10000 r/min for 10 min, pure CBI was obtained.

Preparation of BiVO_4 (BVO): 15 mM $\text{Bi}(\text{NO}_3)_3 \cdot 5 \text{ H}_2\text{O}$ and 15 mM

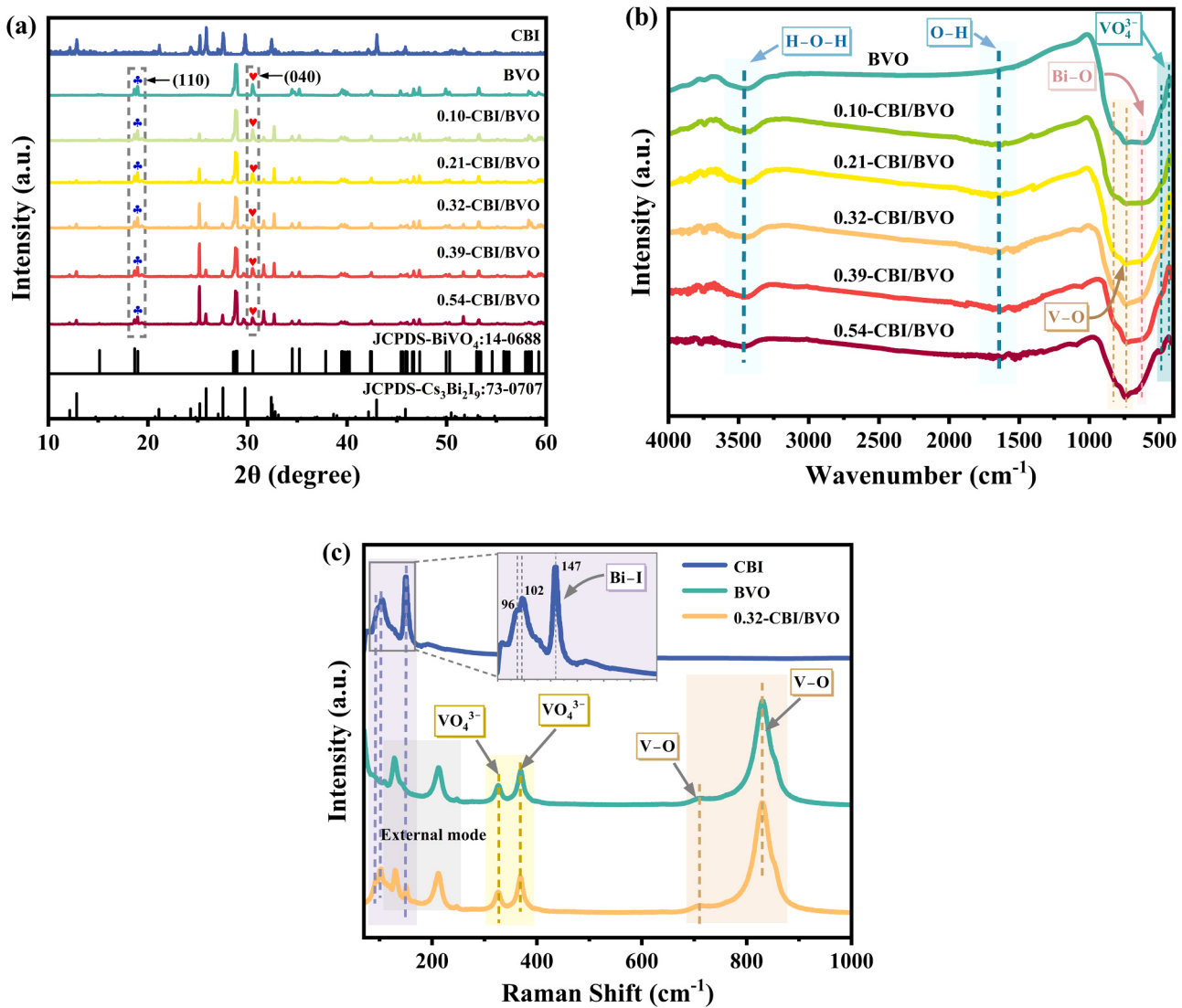


Fig. 1. (a) XRD, (b) FTIR and (c) Raman of CBI, BVO and x-CBI/BVO.

NH_4VO_3 were separately added into 30 mL nitric acid (2 mol/L). After the solution became orange transparent, the pH was adjusted to 1.5 using ammonia and aged for 30 min. Then, the mixture was transferred to 50 mL Teflon-lined steel autoclave and maintained at 165 °C for 12 h. Finally, the obtained sample was calcined at 400 °C for 2 h at a heating rate of 2 °C/min, getting the monoclinic BVO with highly exposed (040) crystal plane.

Preparation of CBI/BVO composite: 200 mg BVO was first dispersed in 200 mL deionized water, and then a certain amount of CBI was added. After stirring under dark conditions for 10 min, the mixture was subjected to xenon lamp illumination for 5 h, obtaining x-CBI/BVO (x represented the actual mass fraction of CBI in CBI/BVO that measured by ICP). Then, the composite photocatalysts were vacuum dried at 60 °C and stored for use. The detailed synthesis process of x-CBI/BVO was presented in Scheme 1.

2.3. Characterizations

The actual mass fraction of CBI in CBI/BVO composite and elements leaching after each photocatalysis were tested by an Avio 200 inductively coupled plasma optical emission spectrometer (ICP-OES). The phase structure and crystallinity of prepared catalysts were measured using a Rigaku D/max-3c X-ray diffractometer (XRD) with Cu target and

$\text{K}\alpha$ as radiation source. The molecular structure of samples was characterized using Cary Eclipse type Fourier transform infrared spectroscopy (FTIR) and Horiba LabRAM HR Evolution Raman instruments. The X-ray photoelectron spectroscopy (XPS) was recorded on a VG-ADES 400 instrument. Morphological analysis was performed using field emission scanning electron microscopy (FE-SEM, Hitachi SU8010), as well as transmission electron microscopy (TEM, JEM-2100 PLUS) equipped with an energy dispersive X-ray spectrometer (EDS). The Cary-50 UV-vis diffuse reflectance spectrometer was employed to test the light absorption characteristics of each sample. The fluorescence characteristics and photogenerated carrier lifetime of photocatalysts were analyzed using the Hitachi F-4500 fluorescence spectrometer (PL). The in situ irradiation X-ray photoelectron spectroscopy (ISI-XPS) was carried on a ESCALAB 250Xi XPS instrument using the excitation source of Al $\text{K}\alpha$ rays ($h\nu = 1486.8 \text{ eV}$) and at the vacuum of $8 \times 10^{-10} \text{ Pa}$. The generation of ROS and RNS during catalytic process was identified by a Brooke A300 electron paramagnetic resonance (EPR) spectrometer. The catalyst photoelectrochemical properties, such as transient photocurrent measurement (I-t), electrochemical impedance spectroscopy (EIS), and Mott-Schottky (M-S) testing, were studied by using a CHI660E electrochemical workstation using 0.1 M Na_2SO_4 as the electrolyte. The internal electric field (IEF) intensity was calculated according to the open circuit potential (OCPT) and I-t, as well as the detailed calculation

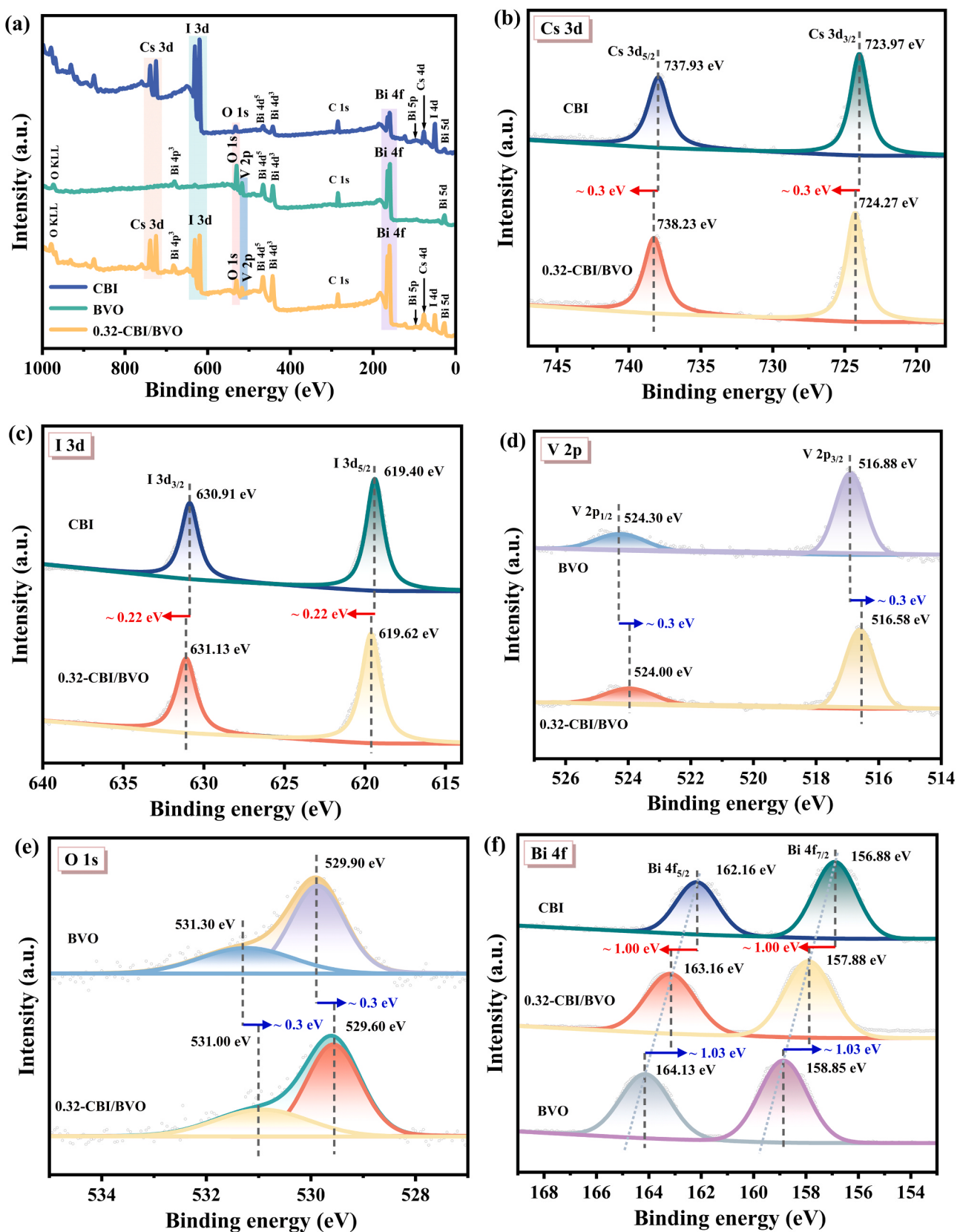


Fig. 2. XPS of CBI, BVO and 0.32-CBI/BVO: (a) full survey spectrum, (b) Cs 3d, (c) I 3d, (d) V 2p, (e) O 1s and (f) Bi 4f.

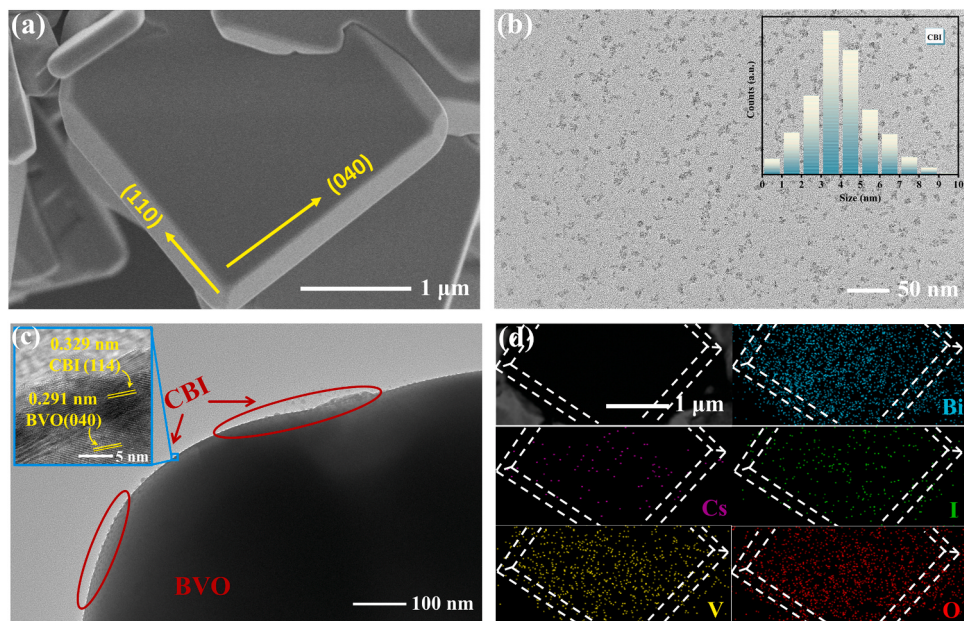


Fig. 3. (a) SEM image of BVO; (b) TEM image of CBI (inset is the grain size distribution of CBI nanocrystal); (c) TEM image of 0.32-CBI/BVO (inset is its HRTEM image); (d) TEM image and element mapping images for Bi, Cs, I, V and O of 0.32-CBI/BVO.

process was provided in [Text S1](#).

2.4. Photocatalytic degradation

According to the UV-vis absorption spectra shown in [Fig. S1](#), nitrate exhibited light absorption in the wavelength range of 260–330 nm, with the highest absorption around 300 nm. Then, a CEL-HXF300D2 Xe lamp with an emission wavelength of 300–780 nm was used as the simulated light source, and the illumination intensity on the reactor surface was determined as 100 mW/cm², which was measured by a spectroradiometer (FZ-A, Photoelectric instrument factory of Beijing Normal University). 100 mg synthesized photocatalyst was dispersed into the mixture of 60 mg/L nitrate and 1 mg/L ATZ solution with the volume of 100 mL. Considering the continuous irradiation of Xe lamp may cause the temperature rising of reaction solution, the circulating condensate was set up in the photocatalytic reaction. From [Fig. S2](#), the temperature of the reaction solution only increased slightly within 120 min of photocatalysis. During the reaction process, 3 mL solution was sampled every 30 min, filtered, as well as the ATZ concentration was monitored on a high-performance liquid chromatography (Shimadzu LC-20A) using the mobile phase of methanol and water (70/30, v/v), the flow rate of 0.8 mL/min, and the detection wavelength of 225 nm. The ATZ intermediates were detected via an Agilent 6470 LC/TQ high-performance liquid chromatography-triple quadrupole mass spectrometer (HPLC-MS). The mobile phase composed of methanol and water in the volume ratio of 85:15 at a flow rate of 0.25 mL/min, and the column temperature was 30 °C. The detection and calculation methods for the concentration changes of nitrate (NO₃⁻-N) and its byproducts, nitrite nitrogen (NO₂⁻-N) and ammonia nitrogen (NH₄⁺-N), were presented in [Supporting Information](#). To understand the effects of each ROS and RNS in catalytic system, tert-butanol (TBA), carbon tetrachloride (CCl₄) [[43](#), [44](#)], ammonium oxalate (AO) and benzoquinone (BQ), were added as the quencher of ·OH, e⁻, h⁺, and ·O₂⁻, respectively. Ferulic acid (FA) can simultaneously capture RNS and ROS (mainly ·O₂⁻, ·OH and hydroxyl peroxides) [[45](#)].

2.5. Theoretical simulation

Based on the first principles of density functional theory (DFT), the work functions of prepared catalysts were calculated using VASP

software to explore the charge transfer law between semiconductor contact interfaces. The transition state search and Gibbs free energy calculation were also conducted on the possible by-products generated during nitrate degradation process, analyzing the nitrate reduction mechanism from a thermodynamic perspective. For simulating the effects of illumination in materials using VASP, computing the properties of materials under electronic excitation was conducted. The GW approximation which can provide accurate description of electrons excited states, was combined with Bethe-Salpeter Equation (BSE) calculations and then been utilized to predict optical properties and electronic excitations. After optimizing the geometric structure using Gaussian 09, the Fukui function of ATZ was calculated to comprehensively understand its electrophilic and nucleophilic active sites, providing data support for its photocatalytic removal mechanism. Additionally, Multiwfn software [[46,47](#)] and VMD (Visual Molecular Dynamics) [[48](#)] software were applied to enhance the data visualization.

3. Results and discussion

3.1. Structure and morphology

XRD was first performed to reveal the phase structure of CBI, BVO, and x-CBI/BVO. As shown in [Fig. 1a](#), the diffraction peaks located at 12.87°, 14.67°, 25.14°, and 27.73° correspond to the (101), (004), (006), and (203) crystal planes of pure CBI (JCPDS NO.73-0707), respectively [[22](#)]. The characteristic peaks at 18.9°, 28.8°, 30.5°, 46.7°, 47.3°, and 53.2° were indexed to the (110), (121), (040), (240), (042), and (161) crystal planes of monoclinic scheelite BVO (JCPDS NO.14-0688) [[49](#)]. In the XRD patterns of x-CBI/BVO, both the typical peaks of CBI and BVO appeared, demonstrating the successful synthesis of CBI/BVO composite, and as the proportion of CBI increased, its peak intensity in the composite catalyst gradually increased. It is worth noting that when x = 0.10, 0.21, 0.32, the diffraction peak intensity of BVO (040) crystal plane was weaker than of pure phase, presumably due to the directional growth of CBI on it. When x continued to increase to 0.39 and 0.54, not only did the peak intensity of (040) crystal plane weaken, but also the peak intensity of (110) crystal plane correspondingly depressed, which should be caused by the excessive CBI loading. The absence of other impurity diffraction peaks indicated the high purity of synthesized material, and the high peak intensity suggested its high

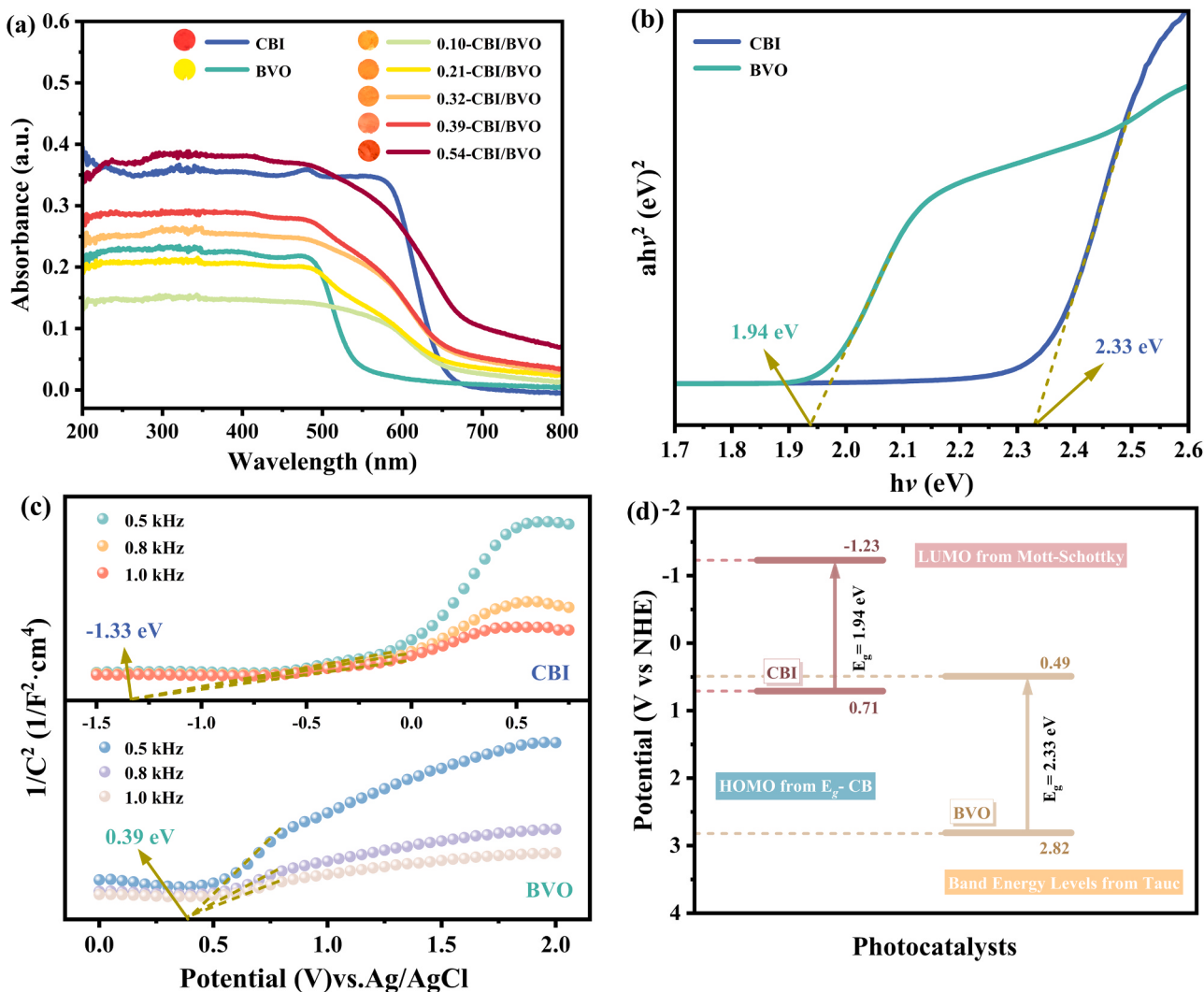


Fig. 4. (a) The UV–vis DRS spectra of CBI, BVO and x-CBI/BVO; (b) The plots of $(\alpha h \nu)^2$ versus photo energy ($h \nu$), (c) M-S and (d) Band gap structure for pure CBI and BVO.

crystallinity. The molecular structure of CBI/BVO were also characterized using FTIR and Raman, as displayed in Fig. 1b and c, both of which indicated the successful combination of CBI and BVO, consistent with the conclusions of XRD.

XPS was employed to analyze the elemental composition, oxidation state, and chemical environment of prepared materials. From the full spectra shown in Fig. 2a, CBI was composed of Cs, Bi and I, as well as a small amount of O probably was attributed to the adsorbed water; BVO was made up of Bi, V and O; 0.32-CBI/BVO presented the typical peaks of Cs, I, V, O and Bi. In the Cs 3d spectra (Fig. 2b), pure CBI exhibited two peaks at 723.97 and 737.93 eV, corresponding to Cs 3d_{3/2} and Cs 3d_{5/2} [23], respectively. Similar characteristic peaks also appeared in the Cs 3d spectrum of 0.32-CBI/BVO, with the difference being that these peaks positively shifted (0.3 eV), indicating a certain decrease in its surface electron density. The I 3d spectrum of CBI (Fig. 2c) presented two characteristic peaks corresponding to I 3d_{5/2} and I 3d_{3/2} at 619.40 eV and 630.91 eV [22]. The typical I 3d peaks of 0.32-CBI/BVO also showed a positive shift, similar to those of Cs 3d, which was caused by electron transfer from CBI to BVO. For BVO, two peaks with binding energies of 516.88 and 524.30 eV were ascribed to V 2p_{3/2} and V 2p_{1/2}, the ones at 529.9 and 531.0 eV corresponded to the lattice oxygen and surface adsorbed oxygen [50], as presented in Fig. 2d–e. For 0.32-CBI/BVO composite, the characteristic peaks attributed to V 2p and O 1s both negatively shifted, indicating an increase in the intensity of the

surface electron cloud, which should be derived from the CBI that closely bounded to BVO. In the Bi 4f spectra shown in Fig. 2f, CBI and BVO exhibited peaks at 156.88 eV and 162.16 eV, as well as 158.85 eV and 164.13 eV, respectively, credited to the Bi 4f_{7/2} and Bi 4f_{5/2} [23,50]. In contrast to CBI, the peaks of Bi 4f in 0.32-CBI/BVO shifted positively, while it underwent a negative shift compared to BVO, which was a comprehensive result of electron transfer from CBI to BVO. XRD, FTIR, Raman, and XPS jointly demonstrated the successful synthesis of CBI/BVO materials, and there was a close connection between the two semiconductors, which was conducive to the subsequent photo-generated carrier transport.

The morphology of prepared photocatalyst was characterized via SEM and TEM, as depicted in Fig. 3. Pure BVO presented a smooth and well-defined decahedral structure with dimensions of 2–3 μm. According to literatures, the top and bottom of the decahedron were (040) crystal planes, and the edges were (110) crystal planes [18,49,51]. According to this, the prepared BVO exhibited highly exposed (040) crystal plane (Fig. 3a). From Fig. 3b, CBI was the nanocrystal structure with a size ranging from 2 to 6 nm. For 0.32-CBI/BVO, its TEM image presented in Fig. 3c revealed that these CBI nanocrystals were tightly deposited on BVO. Zeta potentials (Fig. S3) were further characterized and proved that CBI was positively charged while BVO was negatively charged. It was the electrostatic attraction between two materials led to the tight binding, which was beneficial for the subsequent light

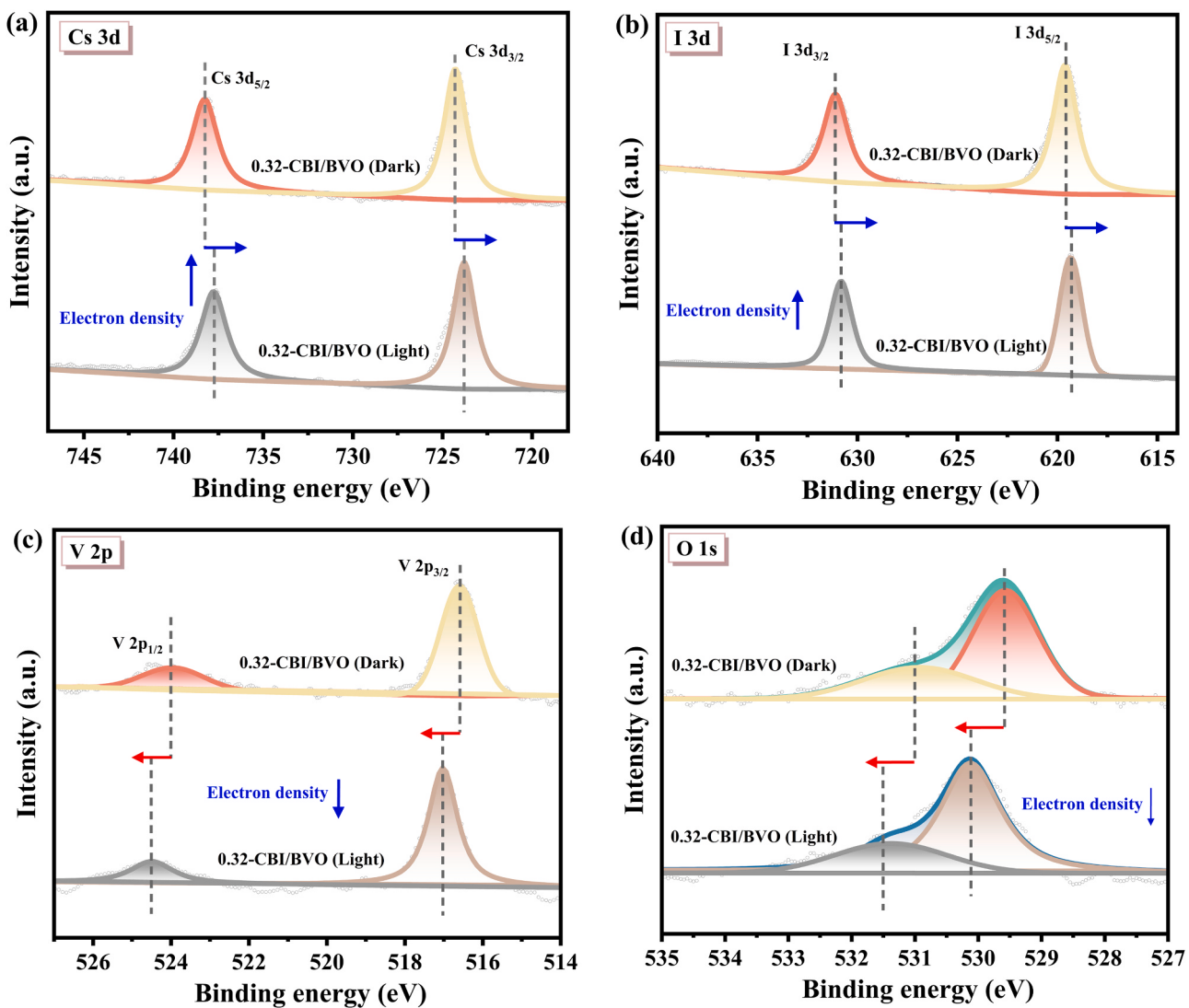


Fig. 5. ISI-XPS spectra of (a) Cs 3d, (b) I 3d, (c) V 2p and (d) O 1s in 0.32-CBI/BVO with and without illumination.

harvesting and photogenerated carrier migration. From the EDS images of 0.32-CBI/BVO (Fig. 3d), the constituent elements Cs and I of CBI were mainly distributed on the top of BVO decahedron. In its corresponding HRTEM image (Fig. 3c inset), the lattice spacing of 0.291 nm matched the (040) plane of BVO, and the lattice space of 0.329 nm corresponded to the (114) plane of CBI. These characterizations undoubtedly demonstrated that the directional deposition of positively charged CBI nanocrystals on the top of BVO decahedron, i.e. the 040 crystal plane, has been achieved. This phenomenon was in agree with the literature reporting that photogenerated electrons tended to accumulate on the (040) crystal plane due to its energy difference with (110) [19,52]. However, as the CBI loading amount continued to increase, the CBI on BVO (040) were polymerized and stacked, and even deposited on the non-target crystal plane (Fig. S4), in agreement with the XRD characterization.

3.2. Light absorption and charge carrier separation ability

The optical properties of CBI, BVO and x-CBI/BVO were characterized by UV-vis DRS, and the results were shown in Fig. 4a. The band edge of pristine BVO was around 520 nm, matched well with its narrow-band semiconductor properties [52]. The CBI optical absorption covered the region of ultraviolet and visible light, ranging from 200 to 625 nm [21]. After combining two materials, the light response range of x-CBI/BVO enlarged, and with the CBI loading increase, the light

absorption intensity improved, which facilitated the photogenerated carriers generation. And the optical absorption properties of all materials matched well with their color. According to the formula $a\hbar v = A(\hbar v - Eg)^{n/2}$, the Tauc curve of catalysts (Fig. 4b) was obtained, in which the band gaps of CBI and BVO were 1.94 and 2.33 eV, respectively [53]. For further exploring the band gap positions, the M-S curves of photocatalysts at different frequencies were tested, respectively. As displayed in Fig. 4c, the positive tangent slope of materials indicated their n-type semiconductor characteristics. Through drawing the intersection of tangent and coordinates, the flat band potentials (V_{fb}) of CBI and BVO were -1.33 and 0.39 eV, that were -1.13 and 0.59 eV (vs. NHE), respectively. Due to the conduction band potential (V_{CB}) of n-type semiconductors was -0.1 eV negative than its V_{fb} [54], the V_{CB} of CBI and BVO were -1.23 and 0.49 eV, respectively. Combined with the band gaps obtained from Fig. 4b, the valence bands were 0.71 and 2.82 eV for CBI and BVO, respectively, that were in accord with the data of XPS-VB shown in Fig. S5. Based on above data, the band gap structure of CBI and BVO were summarized and presented in Fig. 4d.

To analyze the transport and transfer pathways of photoexcited charges within 0.32-CBI/BVO composite, ISI-XPS characterization was conducted. As depicted in Fig. 5a-b, under radiation, the photoelectron peaks of Cs 3d and I 3d on 0.32-CBI/BVO shifted toward lower binding energy compared with those in the corresponding ex-situ spectra, indicating an increase in electron density on CBI. Meanwhile, the

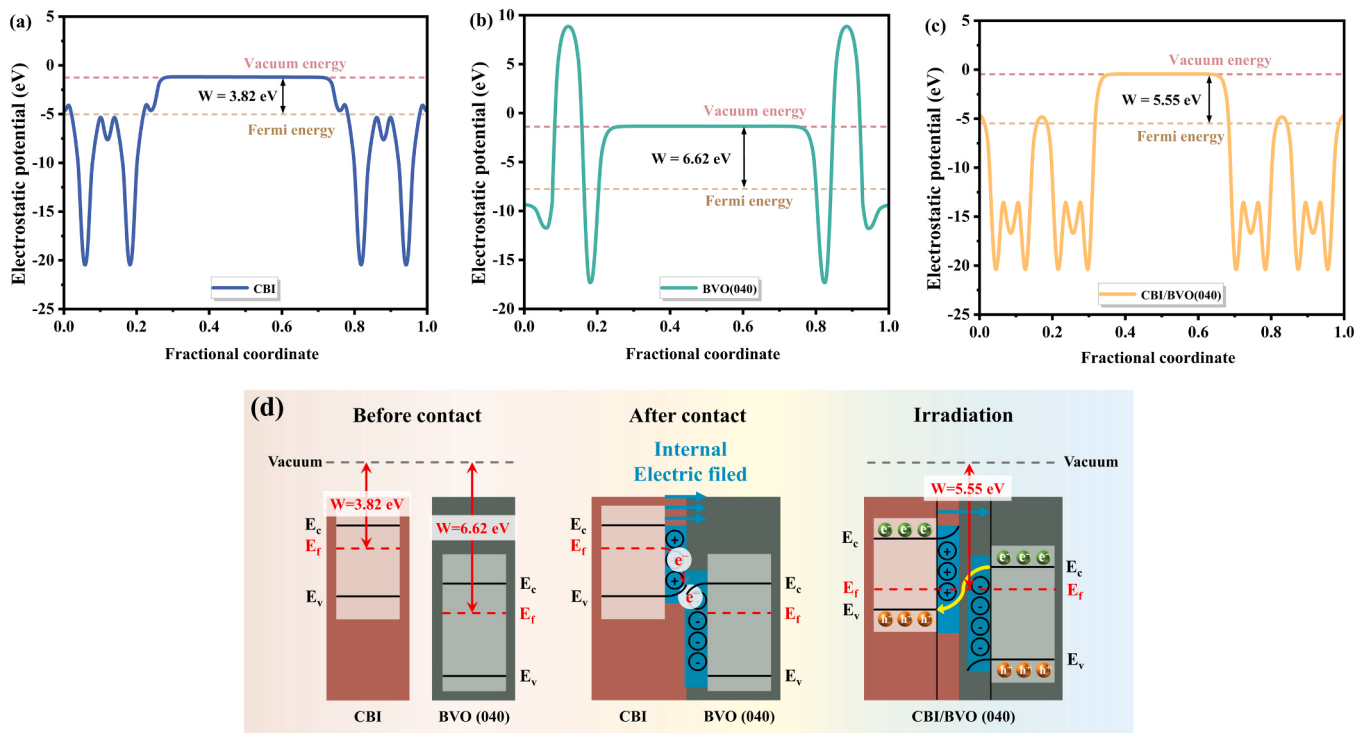


Fig. 6. Work functions: (a) CBI, (b) BVO (040) and (c) CBI/BVO (040); (d) Sketches of internal electric field and charge transfer.

photoelectron signals of V 2p and O 1s moved toward higher binding energy under the same conditions, which suggested the increased hole density on BVO (Fig. 5c-d). The above results jointly proved that under light excitation, photogenerated electrons could transfer from BVO to CBI, while photogenerated holes would migrate from CBI to BVO, demonstrating the successful construction of Z-scheme heterojunction, which effectively maintained the CB electrons on CBI and VB holes on BVO, and consequently improved the redox ability to pollutants.

For intuitively analyzing the photogenerated carriers migration, the work function, which represents the minimum energy required for electrons transfer from the catalyst inside to surface, were calculated through DFT simulation (detailed method was presented in Text S2). Owing to the fact that CBI was deposited on BVO (040) crystal plane, the interaction between them was studied based on the BVO (040) crystal plane. As displayed in Fig. 6a-c, the work functions of pristine CBI, BVO (040), and CBI/BVO (040) heterojunctions were 3.82, 6.62 and 5.55 eV, respectively. Fig. 6d presents the sketches of internal electric field and charge transfer in CBI/BVO (040). According to the principle of semiconductor contact, when two types of semiconductors with different work functions form heterojunctions, electrons will transfer from the material with a small work function to that with the large one until reaching the same Fermi level [55]. Therefore, when CBI and BVO came into contact, the electrons moved from high Fermi level CBI to BVO with low Fermi level, and holes underwent reverse transfer until their Fermi energy levels were equal. Ultimately, CBI accumulated positive charges, and BVO accumulated negative charges, giving birth to an internal electric field (IEF) directed from CBI to BVO. As the charge continued to transfer, the semiconductor bands bent, with positively charged materials (CBI) bending upwards and negatively charged materials (BVO) bending downwards. After photoexcitation, the IEF between CBI and BVO accelerated the photogenerated electrons migration from BVO CB to CBI VB and annihilate them, forming the typical Z-scheme heterojunction, which was conducive to the generation of more ROS with strong redox ability and the consequently enhanced contaminants removal.

The intensity of IEF determines its driving ability for photogenerated

carrier migration [56]. The IEF intensity of x-CBI/BVO were measured using a model developed by Kanata et al. [57], and the detailed calculation process was provided in Figs. S6–7 and Text S1. As presented in Fig. 7a, after setting the IEF intensity of BVO to 1 as standard, the IEF intensities of x-CBI/BVO were 1.64, 20.26, 70.09, 46.77, and 18.96, respectively ($x = 0.10, 0.21, 0.32, 0.39, 0.54$). This result demonstrated the existence of powerful IEF inside 0.32-CBI/BVO, which can drive the directional transfer of photogenerated charge carriers, improve their separation efficiency, as well as increase their number reaching the photocatalyst surface and participate in following photocatalytic reactions. EIS was further tested to analyze the separation and transfer behavior of photogenerated charges within the catalyst, as displayed in Fig. 7b. Among the prepared catalysts, 0.32-CBI/BVO displayed the smallest semicircle diameter, implying the lowest charge transfer resistance. After fitting the Nyquist curve with equivalent circuit (inset of Fig. 7b), the charge transfer resistance (R_{ct} , presented in the inset of Fig. 7b), of 0.32-CBI/BVO was $3820 \Omega/\text{cm}^2$, much lower than that of pure BVO and CBI, indicating the composite has been gifted faster electron transfer capability and the consequently improved photogenerated carriers separation efficiency. Owing to the strongest IEF intensity and lowest R_{ct} , 0.32-CBI/BVO exhibited the highest charge separation efficiency, which was 15.41 times greater than that of pure BVO (presented in Fig. 7c, detailed calculation shown in Fig. S8 and Text S3). The fast and stable photocurrent responses presented in Fig. 7d demonstrated that more photogenerated carriers migrated to the catalyst surface, greatly increasing the possibility for participating in the subsequent photochemical reactions. Photoluminescence (PL) was used to indirectly characterize the separation efficiency of photoinduced carriers. According to Fig. 7e, 0.32-CBI/BVO presented the lowest PL emission peak, which proved that efficient combination between CBI and BVO can significantly suppress the recombination of photogenerated carriers, but excessive CBI could act as new carrier recombination sites and result in enhanced PL peak. The average radiation lifetimes of recombined charge carriers were calculated using TRPL (detailed calculation shown in Text S4). As presented in Table S1 and Fig. 7f, the shortest average radiation lifetimes of recombined charge

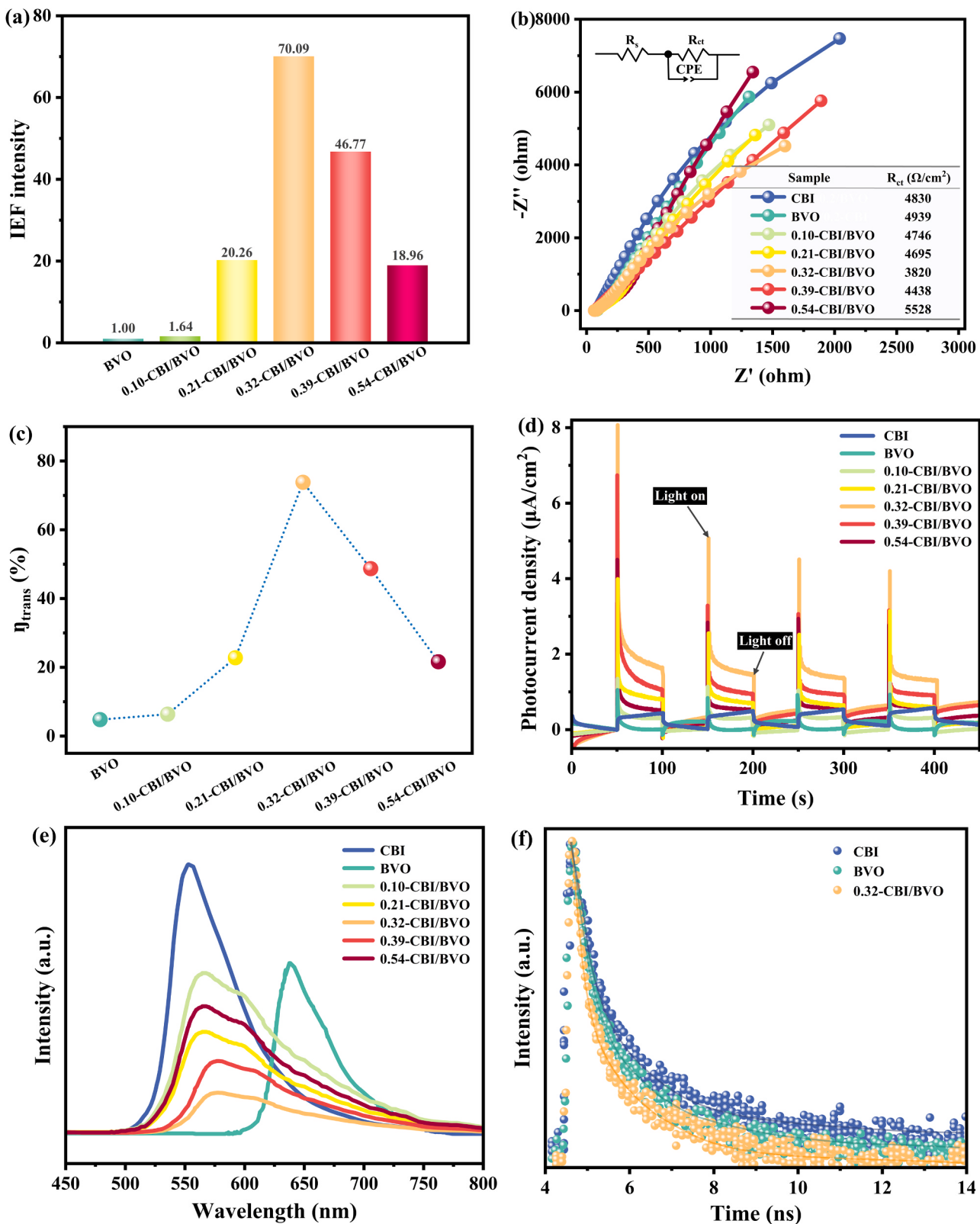


Fig. 7. (a) Tested IEF value (setting the IEF intensity of BVO to 1 as standard), (b) EIS, (c) Charge separation efficiency (η_{trans}), (d) I-t curve, (e) PL and (f) TRPL of CBI, BVO and x-CBI/BVO.

carriers achieved in 0.32-CBI/BVO signified its dissociation of excitons was enhanced, which could cause more carriers rapidly migrating from the bulk phase to the reaction interface.

3.3. Nitrate promoted ATZ removal in Z-Scheme CBI/BVO photocatalytic system

The degradation effect of x-CBI/BVO on ATZ was first investigated,

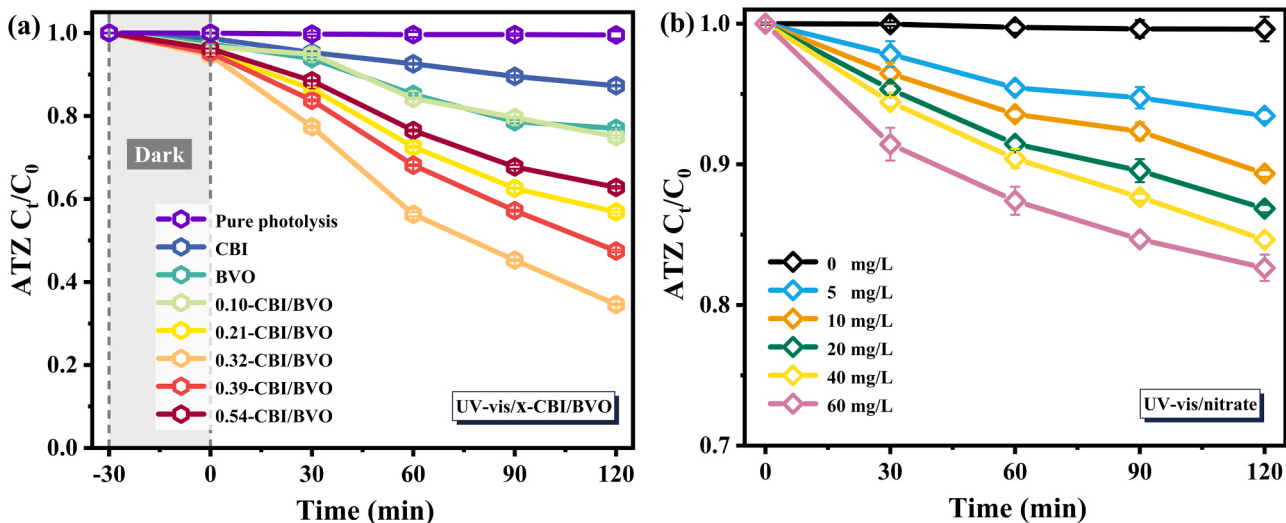


Fig. 8. ATZ degradation (a) using x-CBI/BVO and (b) different concentrations of nitrate under UV-vis ($\lambda > 300$ nm) light.

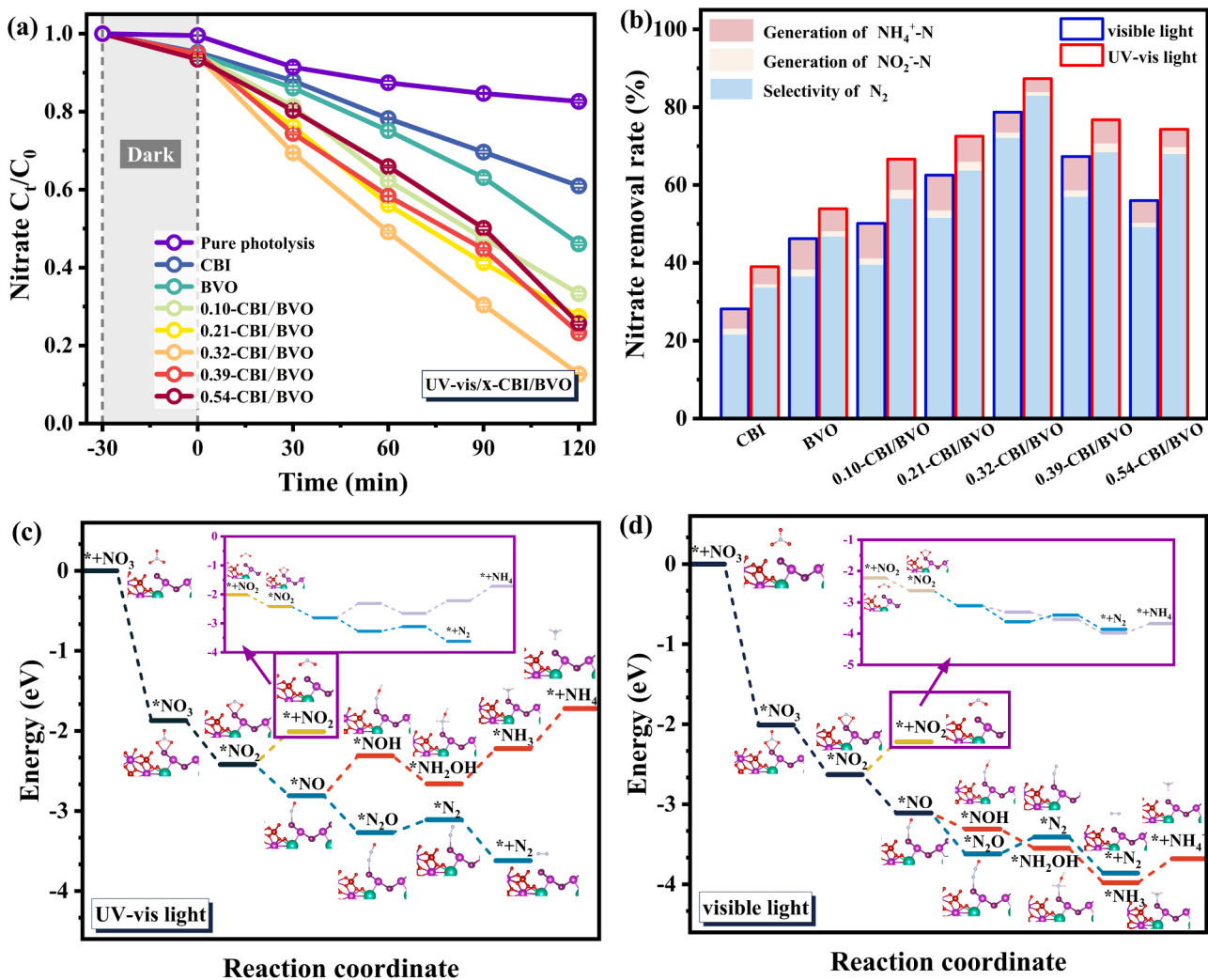


Fig. 9. Nitrate degradation: (a) using x-CBI/BVO under UV-vis light ($\lambda > 300$ nm); (b) intermediates comparison under different lighting conditions; nitrate reduction mechanism under (c) UV-vis ($\lambda > 300$ nm) and (d) visible ($\lambda > 420$ nm) light irradiation.

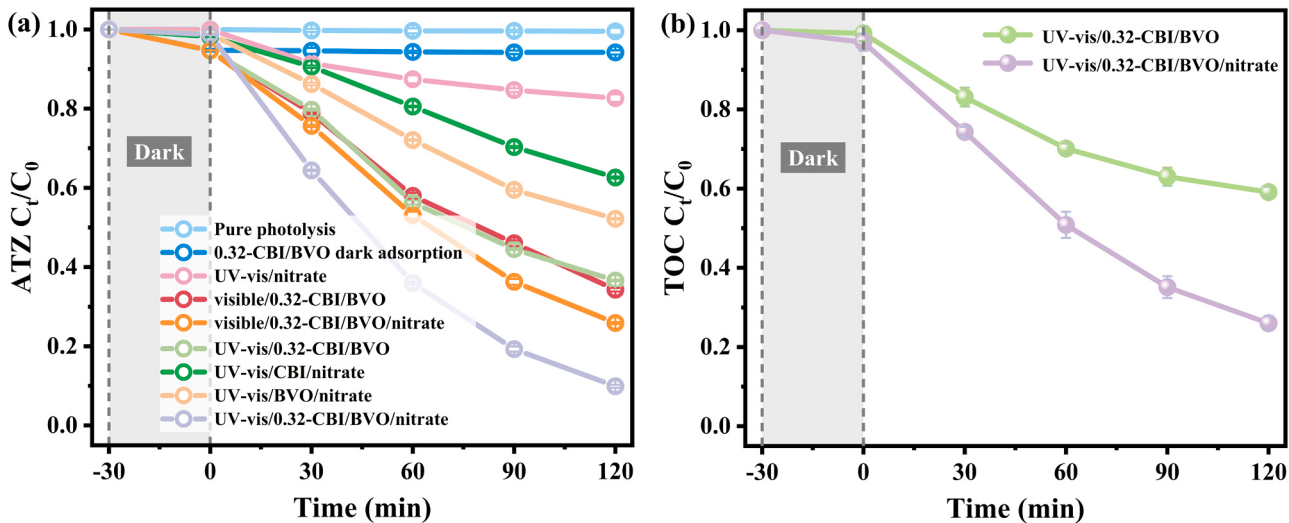


Fig. 10. (a) Degradation and (b) TOC changes of ATZ in different photocatalytic system.

as shown in Fig. 8a. Before illumination, the catalytic system was kept in the dark for 30 min to achieve adsorption-desorption equilibrium between catalyst and contaminates (Fig. S9). After 120 min, 0.32-CBI/BVO exhibited the highest ATZ degradation efficiency, with kinetic constant (Fig. S10) 8.50 and 3.86 times that of pure CBI and BVO, respectively. The enhancement was caused by the strong IEF and high charge separation efficiency within 0.32-CBI/BVO. Fig. 8b presents the variation of ATZ concentration under the action of different concentrations of nitrate. It can be seen that with the nitrate concentration increase, the degradation rates and kinetic constant of ATZ (Fig. S11) increased continuously, which was ascribed to the generation of more active species, such as ROS and RNS, in the system. In the following experiments, nitrate with a concentration of 60 mg/L was used to investigate its promoting effect on ATZ degradation in CBI/BVO catalytic system.

The nitrate removal using x-CBI/BVO under UV-vis ($\lambda > 300$ nm) was investigated and the performances were compared with those under visible light ($\lambda > 420$ nm). As shown in Fig. 9a, both the catalyst dark adsorption (Fig. S12) and pollutant itself photodegradation did not account for a large proportion of nitrate removal, as well as the catalytic system under visible light irradiation also exhibited similar trend (Fig. S13). After adding catalysts, the nitrate degradation rates improved significantly, that was caused by the reduction of photoinduced electrons originated from catalyst excitation. Among them, 0.32-CBI/BVO displayed the highest nitrate removal efficiency, whose kinetic constant was 4.35 and 2.78 times that of CBI and BVO (Fig. S14), respectively, reflecting the significance of increasing the photogenerated carriers number and intensifying their separation to contaminate decomposition. The fate of nitrate degradation products were also analyzed and compared (detailed characterization and calculations presented in Text S5). From Fig. 9b, it can be observed that although the lighting conditions were different, the variability trends of intermediate products were similar. As shown in Fig. S15, the NO_2^- -N generation first increased and then decreased, but overall remained at a lower level, which was attributed to the fact that NO_3^- can be converted to NO_2^- ($E(\text{NO}_3^-/\text{NO}_2^-) = 0.94$ V) and then further reduced to N_2 ($E(\text{NO}_2^-/\text{N}_2) = 1.45$ V). The NH_4^+ -N concentration displayed a cumulative upward trend, which was because in addition to the direct reduction of NO_3^- to NH_4^+ ($E(\text{NO}_3^-/\text{NH}_4^+) = 1.20$ V), the NO_2^- produced by NO_3^- reduction can also be converted to NH_4^+ ($E(\text{NO}_2^-/\text{NH}_4^+) = 0.90$ V). Overall, N_2 was the product with the highest generation yield. The N_2 selectivity of 0.32-CBI/BVO under UV-vis and visible light excitation was 95.25% and 91.88%, respectively, indicating that most NO_3^- is reduced to N_2 ($E(\text{NO}_3^-/\text{N}_2) = 1.25$ V [58]). Based on the transition state theory and thermochemical cycle principle, DFT was conducted to calculate the

Gibbs free energy of active intermediates and thus propose the nitrate reduction mechanism of CBI/BVO (040) under different wavelength excitation (Figs. 9c and 9d). First, NO_3^- was adsorbed on the active sites of catalyst surface and produced $^*\text{NO}_3$, which could be further reduced to $^*\text{NO}_2$ and $^*\text{NO}$ through N-O cleavage. The generated $^*\text{NO}$, as a branch, was a key intermediate for the formation of N_2 or NH_4^+ . One path was the continuous hydrogenation of $^*\text{NO}$ to produce $^*\text{NOH}$, $^*\text{NH}_2\text{OH}$ and finally form $^*\text{NH}_4^+$. Another pathway was the surface bound $^*\text{NO}$ dimerized with NO_{aq} which was desorbed and dissolved in solution, forming $^*\text{N}_2\text{O}$ which can be easily reduced to $^*\text{N}_2$ and desorb from the catalyst surface. It is worth noting that in the CBI/BVO (040) catalytic system excited by UV-vis light, the Gibbs free energy of $^*\text{N}_2\text{O}$ generation ($\Delta G(^*\text{N}_2\text{O}) = ^*\text{N}_2\text{O} - ^*\text{NO} = -0.46$ eV) was lower than that of $^*\text{NOH}$ ($\Delta G(^*\text{NOH}) = ^*\text{NOH} - ^*\text{NO} = 0.5$ eV), indicating that N_2 was more thermodynamically formed than NH_4^+ , which was consistent with the experimental results. When the light source was visible light (Fig. 9d), the Gibbs free energy of $^*\text{N}_2\text{O}$ generation (-0.51 eV) exhibited no obvious change, suggesting N_2 was still an easily generated product. But the Gibbs free energy of $^*\text{NOH}$ generation (-0.21 eV) declined significantly, indicating the NH_4^+ production energy barrier decreased and thus exhibiting increased yield, which was in accord with the experimental results.

The degradation of ATZ improved by nitrate in CBI/BVO photocatalytic system were studied. First, batch experiments were performed and the best photocatalytic conditions were determined to pH of 5, ATZ initial concentration of 1 mg/L, and catalyst dosage of 1 g/L (Fig. S16-18). As shown in Fig. 10a, compared with visible/0.32-CBI/BVO, the visible/0.32-CBI/BVO/nitrate exhibited increased ATZ removal rate, which was attributed to the promotion of nitrate as efficient electron acceptor to the photogenerated carriers separation within 0.32-CBI/BVO catalyst. The enhanced catalytic activity of UV-vis/0.32-CBI/BVO/nitrate in comparison with UV-vis/CBI/nitrate and UV-vis/BVO/nitrate demonstrated the importance of excellent photocatalyst design for pollutant removal. Among the catalytic systems, UV-vis/0.32-CBI/BVO/nitrate displayed the best ATZ degradation performance, with a kinetic constant 14.46 times that of UV-vis/nitrate and 2.37 times that of UV-vis/0.32-CBI/BVO (Fig. S19). The enhanced light harvesting and strong IEF of 0.32-CBI/BVO composite increased the number of photogenerated charge carriers and their migration ability, which was conducive to the production of more active species and thus rapid contaminates removal. The coexisting nitrate can serve as electron quenchers to promote the separation of photoinduced charge carriers, and on the other hand, the $\cdot\text{OH}$ and RNS generated by its photolysis can enhance the ATZ removal. The TOC change in two photocatalytic system

Table 1

The comparison of photocatalytic ATZ removal in different studies.

Photocatalyst	Light condition	Catalyst (g/L)	ATZ (ppm)	Dominant reactive species	Time (min)	Conversion (%)	k (min ⁻¹)	TOC (%)	Ref.
BiOBr/UiO-66	300 W Xe lamp $\lambda > 400$ nm	0.5	5	•OH, h ⁺	240	88.00	0.73×10^{-2}	-	[59]
AC/g-C ₃ N ₄ composites	300 W Xe lamp $\lambda > 400$ nm	1.0	5	•OH, •SO ₄ ⁻	120	78.76	3.76×10^{-2}	-	[60]
CdS/RGO/g-C ₃ N ₄	350 W Xe lamp	0.44	10	•OH, h ⁺ , •O ₂ ⁻	300	90.50	0.71×10^{-2}	-	[61]
NF-TiO ₂ NWs	15 W fluorescent lamp $\lambda > 420$ nm	1.0	5	-	360	> 60.00	-	-	[62]
Bi ₂ WO ₆ -g-C ₃ N ₄ /PVDF	500 W Xe lamp	-	5	•OH, h ⁺ , •O ₂ ⁻	360	72.41	0.33×10^{-2}	46.57	[63]
TiO ₂ @LaFeO ₃ /PMS	200 W LED lamp $760 > \lambda > 410$ nm	0.5	2.5	¹ O ₂ , h ⁺ , •O ₂ ⁻ , •OH, •SO ₄ ⁻	90	100.00	-	37.04	[64]
0.32-CBI/BVO	300 W Xe lamp	1.0	1	•OH	120	65.41	0.85×10^{-2}	40.88	This work
0.32-CBI/BVO/nitrate	780 > λ > 300 nm	-	-	•OH, RNS	120	90.10	2.02×10^{-2}	73.99	-

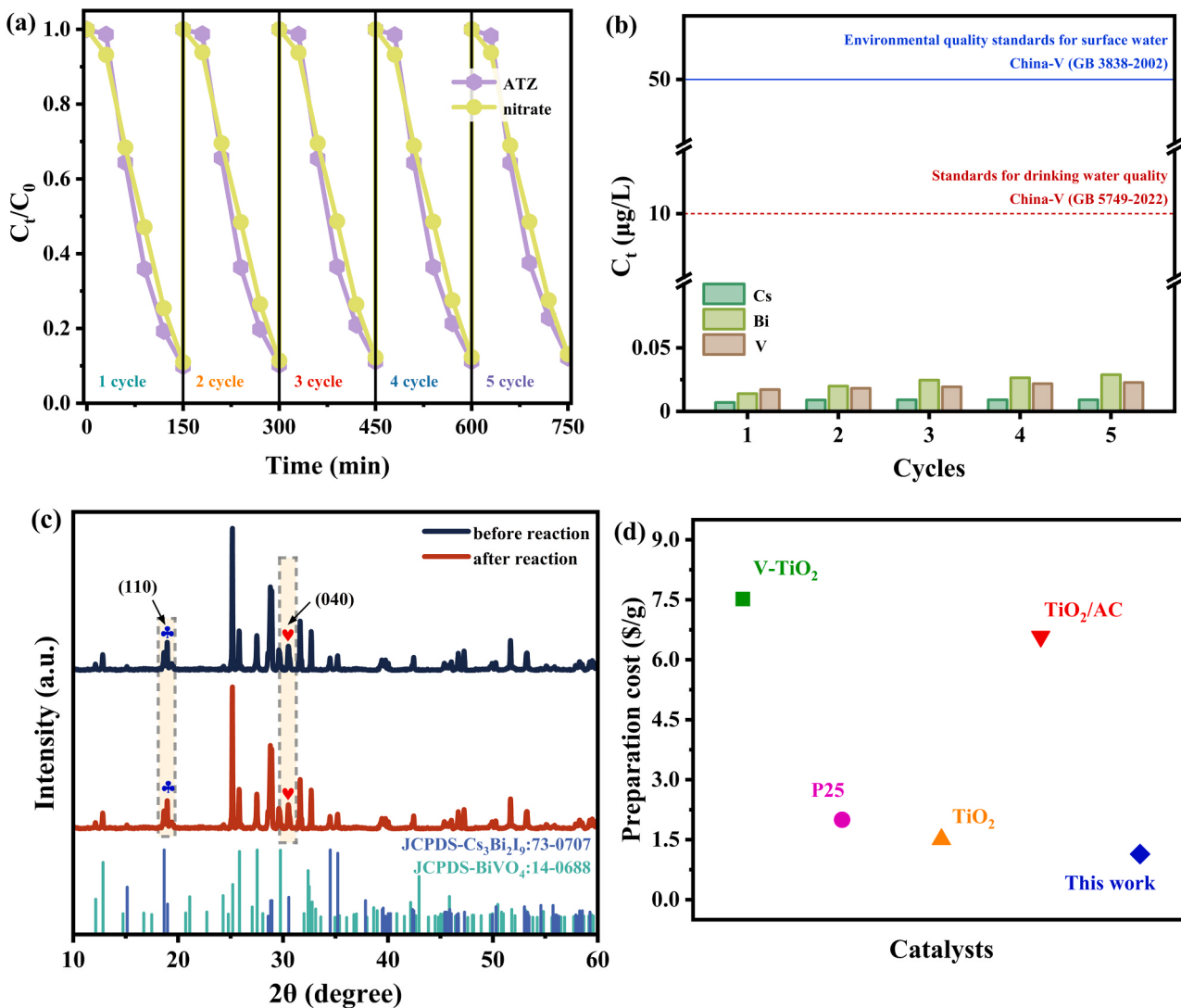


Fig. 11. (a) Recycling test; (b) The monitoring of Cs, Bi and V dissolution in each cycle; (c) XRD pattern of 0.32-CBI/BVO before and after photocatalysis; (d) Comparison of preparation cost for different catalysts.

were also performed. As displayed in Fig. 10b, the ATZ mineralization rate in UV-vis/0.32-CBI/BVO/nitrate system was 73.99%, much higher than that of UV-vis/0.32-CBI/BVO (40.88%), coincided with their photocatalytic degradation performance. This work has also been compared with the results in literatures, as shown in Table 1 [59–64]. Despite different photocatalytic experimental conditions, such as light

irradiation, catalyst dosage, ATZ concentration, etc., the CBI/BVO catalytic system with nitrate coexistence still exhibited satisfactory degradation and mineralization ability for ATZ. The nitrate changes in prepared systems were monitored. As presented in Fig. S20 and Fig. S21, the coexistence of ATZ accelerated the nitrate reduction by UV-vis/0.32-CBI/BVO, which was because ATZ served as efficient hole

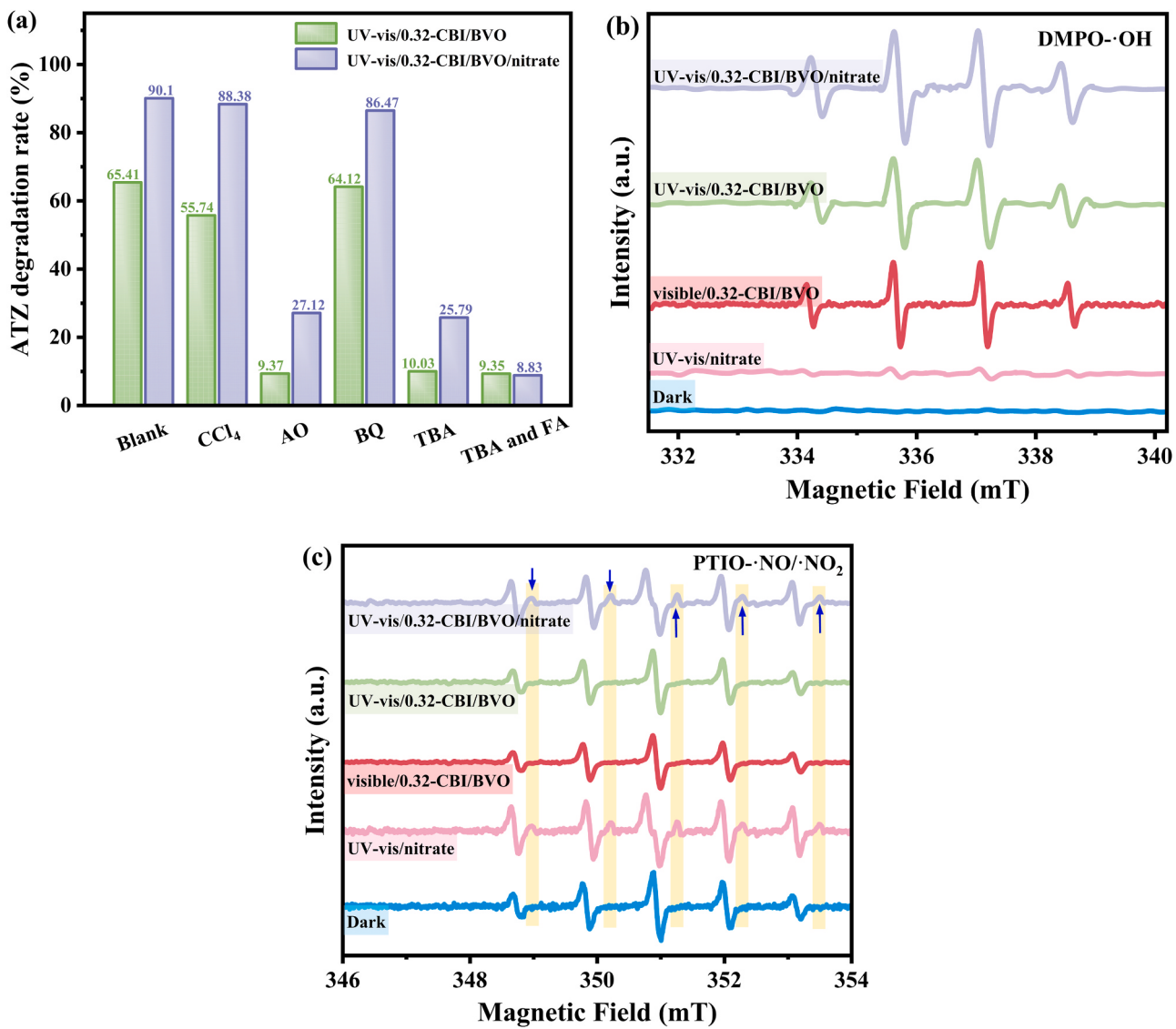


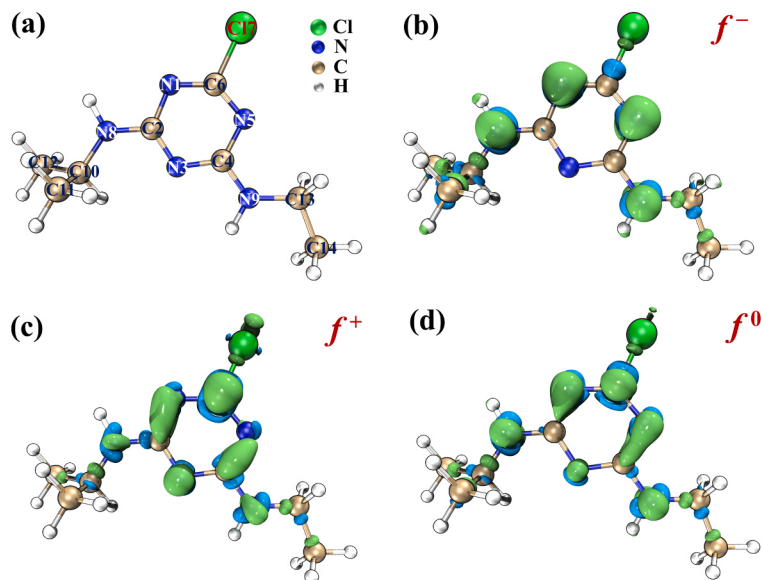
Fig. 12. (a) Radical trapping experiments; EPR chromatograms: (b) DMPO-·OH; (c) PTIO-·NO/·NO₂.

capturers owing to its high electrical density groups, enhancing carrier separation and promoting reduction reactions. Similar nitrate degradation rates and nitrogen selectivity comparison between this paper and literatures was shown in Table S2, reflecting the superiority of UV-vis/0.32-CBI/BVO/nitrate system. The UV-vis/0.32-CBI/BVO/nitrate system also presented efficient degradation toward TC and SMX, demonstrating its advantage in various pollutants synergetic removal (Fig. S22).

The stability and reusability of photocatalysts are of great significance for their practical applications. Fig. 11a shows the cyclic degradation of ATZ and nitrate in UV-vis/0.32-CBI/BVO/nitrate system. The removal rate of ATZ and nitrate remained at a high level even after 5 cycles, proving its good stability and reusability. From Fig. 11b, only a very small amount of Cs, Bi and V were leached during this process. Comparing the XRD patterns (Fig. 11c) of 0.32-CBI/BVO before and after photocatalysis, both the characteristic peaks of CBI and BVO were observed, and there was no significant change in the (110) and (040) crystal plane peaks, reflecting their good chemical stability. The catalyst preparation cost was further calculated and compared with literature data [65–68]. As presented in Fig. 11d, the synthesis cost of 0.32-CBI/BVO was lower than those reported in literatures, suggesting its potential in practical application.

3.4. Proposed photocatalytic mechanism

To investigate the role of each ROS and RNS, the radical trapping experiments were carried out and the results were presented in Fig. 12a. The TBA introduction maximally restricted the degradation of ATZ in UV-vis/0.32-CBI/BVO/nitrate photocatalytic system, which was similar to the addition of AO, proving ·OH that mostly originated from the reaction of photogenerated holes with OH/H₂O was the main species in system. CCl₄ and BQ hardly inhibited the ATZ removal, which was ascribed to the fact that the photogenerated electrons produced by catalyst were mainly involved in the nitrate reduction. Ferulic acid (FA) can capture both RNS and ROS (mainly ·O₂⁻, ·OH and hydroxyl peroxides). Based on the minor role of ·O₂⁻ and hydroxyl peroxides in this experiment, the trapping of ·OH and RNS by FA was investigated. TBA was first added to achieve complete ·OH removal (Fig. S23), and then FA was added for RNS capture. The declined UV-vis/0.32-CBI/BVO/nitrate photocatalytic activity demonstrated the important role of RNS in contaminants decomposition. In summary, ·OH and RNS were the main species responsible for ATZ degradation in UV-vis/0.32-CBI/BVO/nitrate system. In the UV-vis/0.32-CBI/BVO catalytic system, the AO and TBA adding maximally depressed ATZ removal, proving the significance of ·OH in pollutant decomposition. After CCl₄ captured electrons, the



No.(Atom)	Hirshfeld charges			condensed Fukui functions		
	$q(N)$	$q(N+1)$	$q(N-1)$	f^-	f^+	f^0
1(N)	-0.2226	-0.3054	-0.0975	0.1251	0.0828	0.1039
2(C)	0.1573	0.1042	0.1822	0.0248	0.0531	0.039
3(N)	-0.2252	-0.3203	-0.1954	0.0298	0.0951	0.0625
4(C)	0.1568	0.0859	0.1837	0.027	0.0708	0.0489
5(N)	-0.2146	-0.2759	-0.0884	0.1263	0.0613	0.0938
6(C)	0.1379	-0.0012	0.1709	0.033	0.139	0.086
7(Cl)	-0.0878	-0.2452	0.0143	0.1021	0.1574	0.1297
8(N)	-0.0827	-0.1183	0.0218	0.1045	0.0356	0.07
9(N)	-0.0852	-0.1277	-0.0034	0.0817	0.0425	0.0621
10(C)	0.04	0.033	0.0542	0.0142	0.007	0.0106
11(C)	-0.0911	-0.1006	-0.0701	0.021	0.0095	0.0153
12(C)	-0.0858	-0.0951	-0.0729	0.0128	0.0093	0.0111
13(C)	0.0088	-0.004	0.0233	0.0145	0.0128	0.0137
14(C)	-0.0824	-0.0934	-0.0716	0.0108	0.011	0.0109

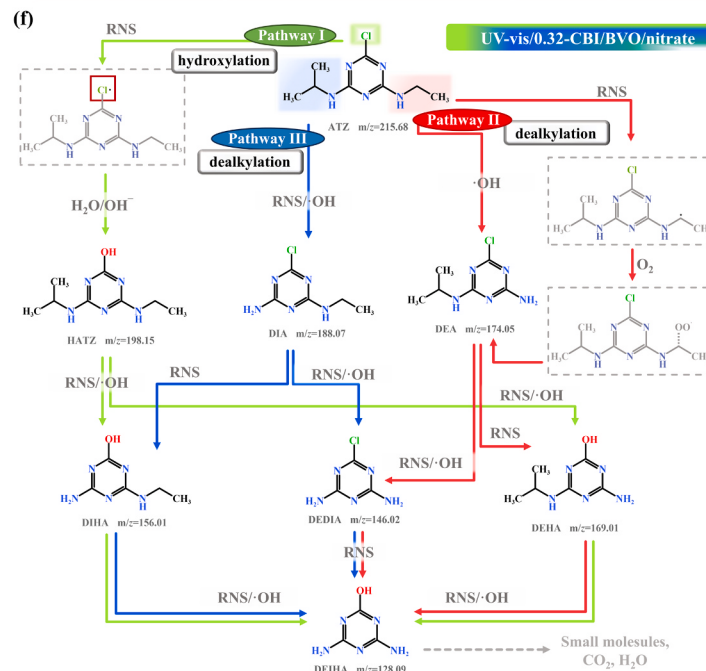


Fig. 13. (a) Optimized ATZ molecule structure and corresponding atomic number; Computed isosurfaces of (b) f^- , (c) f^+ and (d) f^0 ; (e) Calculated Hirshfeld charge distribution of ATZ and condensed Fukui function values; (f) Proposed degradation pathways of ATZ in UV-vis/0.32-CBI/BVO/nitrate.

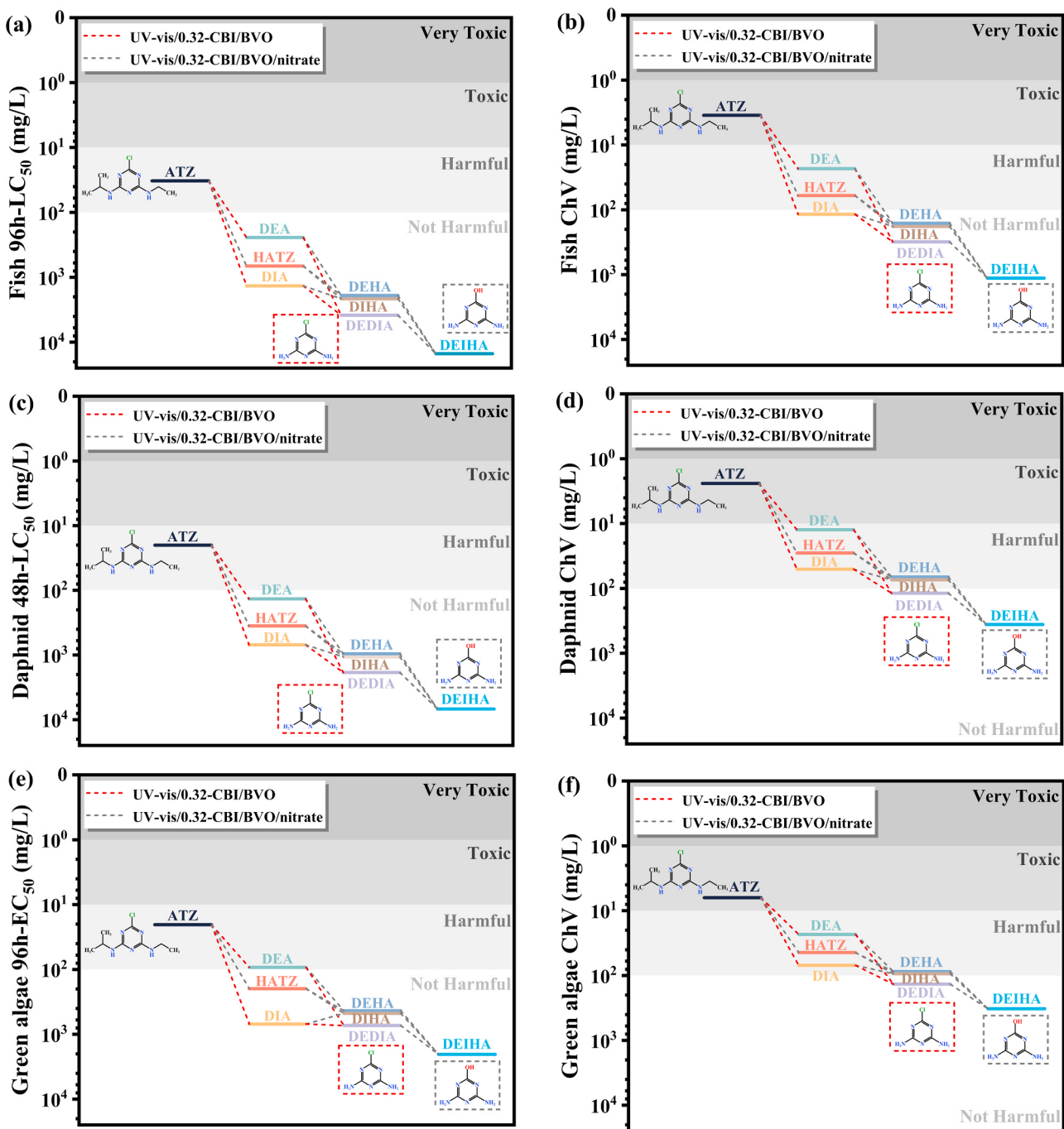
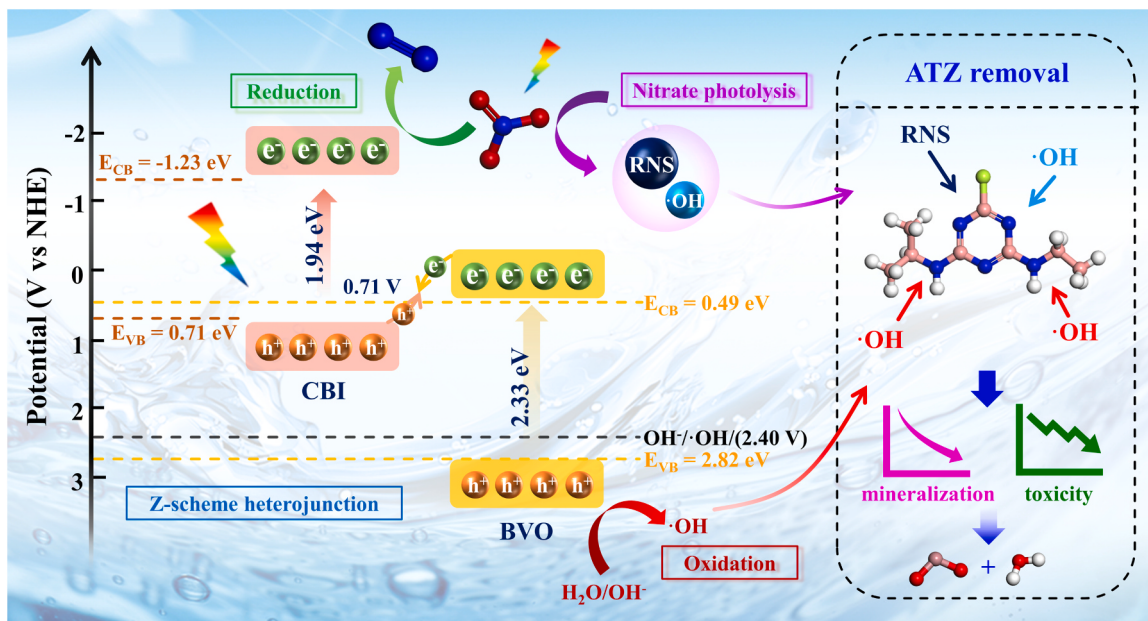


Fig. 14. Estimated acute and chronic toxicity toward (a-b) fish, (c-d) daphnid and (e-f) green algae for ATZ and its intermediates.

photocatalytic performance was reduced to a certain degree, implying that electrons were also important active species. BQ and FA possessed almost no effect on the ATZ degradation, indicating the minor role of $\cdot\text{O}_2^-$ and RNS in UV-vis/0.32-CBI/BVO system. EPR was also conducted to monitor the generation of $\cdot\text{OH}$ and $\cdot\text{NO}/\cdot\text{NO}_2$ (Figs. 12b and 12c). In the dark state, no or only signals from capture agent were found. Under UV-vis light excitation, nitrate underwent photolysis and produced the signals of PTIO- $\cdot\text{NO}/\cdot\text{NO}_2$, proving the formation of $\cdot\text{NO}/\cdot\text{NO}_2$ [69]. The characteristic peak of DMPO- $\cdot\text{OH}$ was relatively weak. From the Gibbs free energy step diagram of free radicals generated from nitrate photolysis shown in Fig. S24, the Gibbs free energy of $\cdot\text{NO}_2$ generation ($\Delta G(\cdot\text{NO}_2) = \cdot\text{NO}_2 - \cdot[\text{NO}_3^-]^* = -0.75 \text{ eV}$) was lower than that of $\cdot\text{O}^-$ generation ($\Delta G(\cdot\text{O}^-) = \cdot\text{O}^- - \cdot[\text{NO}_3^-]^* = -0.45 \text{ eV}$), indicating nitrate photolysis was more thermodynamically prone to the $\cdot\text{NO}_2$ production.

Due to the absence or inability to excite nitrates, no PTIO- $\cdot\text{NO}/\cdot\text{NO}_2$ peak was observed in the UV-vis/0.32-CBI/BVO and visible/0.32-CBI/BVO/nitrate systems, while the DMPO- $\cdot\text{OH}$ peaks came from the $\cdot\text{OH}$ generated by catalyst photoexcitation. In the UV-vis/0.32-CBI/BVO/nitrate system, there were both the peaks of PTIO- $\cdot\text{NO}/\cdot\text{NO}_2$ and DMPO- $\cdot\text{OH}$, which matched well with its high catalytic activity.

Hirshfeld charges and Fukui functions were calculated to identify the atoms that were easy to be attacked by active species on ATZ, as displayed in Fig. 13a-e. According to reports, the isosurfaces f^- , f^+ and f^0 can directly reflect the atoms electrophilicity, nucleophilicity, and vulnerability to free radicals [70]. It can be seen that the 1 N, 5 N, 7 Cl, and 8 N atoms were apt to attract attacks from electrophilic $\cdot\text{OH}$ and RNS owing to their high f^- values. The 1 N, 2 C, 3 N, 4 C, 5 N, 6 C, 7 Cl,



Scheme 2. Proposed photocatalytic mechanism for ATZ degradation in UV-vis/0.32-CBI/BVO/nitrate system.

8 N and 9 N possessed high f^+ values, suggesting that they were more susceptible to react with nucleophile. In addition, the high f^0 values of ATZ located at 1 N, 5 C, 6 C, 7Cl, 8 N and 9 N, respectively, which indicated that these sites were prone to respond to ·OH with dual characteristics of electrophilicity and free radicals. Based on the Fukui functions, HPLC-MS analysis (Fig. S25) and previous reports [60, 64, 70–71], the ATZ degradation pathway was analyzed and presented in Fig. 13f. Table S3 lists the mass-to-charge ratio and molecular structures of detected intermediates. In the UV-vis/0.32-CBI/BVO/nitrate system, three ATZ degradation pathways, namely dechlorination hydroxylation, side chain attack ethylamine dealkylation, and side chain attack isopropylamine dealkylation, have been proposed. In Path I, ATZ was first attacked by RNS, forming an organic radical cation ($[C_8H_{14}ClN_5]^+$). Owing to the high f^+ of ATZ-7Cl, it was vulnerable to react with typically nucleophilic species H_2O , generating the dechlorination-hydroxylation product HATZ [72]. Under the action of RNS, and ·OH, HATZ can occur depropylation and depropylation to form DIHA and DEIHA, or undergo the opposite processes to obtain DEHA and DEIHA. Via Path II, the ethylamino group on ATZ side chain was attacked and occurred dealkylation to generate DEA. Two processes could cause this result. One was the attack of electrophilic ·OH on 9 N-13 C, both of which had high f^- , achieving dealkylation and the formation of DEA. Another approach was to attack the chain alkyl groups of ATZ with electrophilic RNS, and then induced the production of intermediate product DEA through dissolved oxygen. The isopropylamine group on the side chain of DEA can depropyl to form DEDIA, which was further attacked by RNS and dechlorinated to form DEIHA. If the process of dechlorination followed by depropylation occurred, DEHA and DEIHA would be generated. For Path III, ATZ first removed the side chain propyl group and generated DIA. DIA could first deethylate and then dechlorinate, giving birth to DEDIA and DEIHA, or dechlorinate first and then dechlorinate to produce DIHA and DEIHA. Under the attack of RNS and ·OH, these typical intermediates were further degraded into small molecule, such as CO_2 and H_2O . The ATZ degradation pathway in UV-vis/0.32-CBI/BVO system was also investigated and compared with that in UV-vis/0.32-CBI/BVO/nitrate. As presented in Fig. S26, ATZ and intermediates DEA and DIA did not undergo further dechlorination-hydroxylation reaction, proving the positive role of RNS derived from nitrate photolysis to ATZ degradation.

Fish, daphnia and green algae, as typical group model organism, are

often used by the United States Environmental Protection Agency to predict the aquatic toxicity of chemicals [70,73]. To understand the toxicity variations of ATZ and its intermediate in UV-vis/0.32-CBI/BVO/nitrate and UV-vis/0.32-CBI/BVO system, the acute and chronic toxicity to these trophic aquatic organisms were evaluated based on ECOSAR structure-activity relationship. As depicted in Fig. 14 and Table S4, as the photocatalysis continued, both the LC₅₀/EC₅₀ and ChV values of intermediates increased, proving the toxicity were decreasing. In the UV-vis/0.32-CBI/BVO/nitrate system, DEDIA was further decomposed into less toxic DEIHA, demonstrating its higher detoxification ability. The above phenomenon jointly suggested that the UV-vis/0.32-CBI/BVO/nitrate photocatalytic system can not only efficiently decompose and mineralize ATZ, but also reduce the toxicity of its intermediates, thereby reducing impact on the environment and ecology.

Based on above experiments and data analysis, the mechanism of nitrate promoting ATZ degradation in CBI/BVO photocatalytic system was proposed, as shown in Scheme 2. After UV-vis light ($\lambda > 300$ nm) irradiation, both CBI and BVO were excited and produced photo-generated charge carriers. The electrons of BVO recombined with CBI holes under the action of built-in electric field, accelerating the photo-induced carrier separation and simultaneously releasing CBI CB electrons with strong reducing ability ($E_{CB} = -1.23$ eV vs. NHE) and BVO VB holes with powerful oxidation ($E_{VB} = 2.82$ eV vs. NHE). The CBI CB electrons promoted the nitrate reduction, meanwhile, nitrate was photolyzed and produced RNS, which worked together with the ·OH originated from the BVO VB holes oxidation, finally achieving efficient degradation, mineralization, and detoxification of ATZ.

4. Conclusions

In summary, the enhancement effect of nitrate on ATZ removal in Z-scheme CBI/BVO photocatalytic system was systematically studied, and its synergistic catalytic mechanism was deeply analyzed. The CBI/BVO composite achieved the maximum number of photogenerated carriers under the action of Z-scheme heterojunction, and the release of CBI electrons and BVO holes endowed these photoinduced carriers with powerful redox ability. Researches shown that the nitrate-mediated RNS selectively attacked the electron donating groups of ATZ and its intermediates, which combined with the oxidation of ·OH generated from

CBI/BVO excitation, collaboratively achieving efficient ATZ degradation, mineralization and detoxification. This work highlights the important role of ·OH and RNS-mediated reduction and oxidation in the efficient removal of ATZ. Similar studies can also be extended to the removal of other pollutants with electron donating structures coexisting with nitrate, providing a new solution for the remediation of water bodies polluted by various contaminates.

CRediT authorship contribution statement

Xinyu Duan: Writing – original draft, Investigation, Conceptualization. **Huiping Jia:** Writing – original draft, Investigation. **Tingting Cao:** Data curation. **Hongbin Yu:** Methodology. **Yanan Zhang:** Software. **Ying Lu:** Writing – review & editing, Supervision. **Dandan Zhou:** Resources.

Declaration of Competing Interest

The authors declare that they have no known competing financial interests or personal relationships that could have appeared to influence the work reported in this paper.

Data availability

No data was used for the research described in the article.

Acknowledgements

This work was supported by the Science and Technology Project of Jilin Province (20220101167JC; 20220101162JC), the Scientific Research Project of Jilin Provincial Department of Education (JJKH20231323KJ), the Fundamental Research Funds for the Central Universities (2412022ZD055), and the National Natural Science Foundation of China (51778117; 52200043). The work was carried out at Shanxi Supercomputing Center of China, and the calculations were performed on TianHe-2.

Appendix A. Supporting information

Supplementary data associated with this article can be found in the online version at [doi:10.1016/j.apcatb.2024.124016](https://doi.org/10.1016/j.apcatb.2024.124016).

References

- [1] N. Graziano, M.J. McGuire, A. Roberson, C. Adams, H. Jiang, N. Blute, 2004 national ATZ occurrence monitoring program using the Abraxis ELISA method, *Environ. Sci. Technol.* 40 (2006) 1163–1171, <https://doi.org/10.1021/es051586y>.
- [2] A. Koroša, P. Auersperger, N. Mali, Determination of micro-organic contaminants in groundwater (Maribor, Slovenia, *Sci. Total Environ.* 571 (2016) 1419–1431, <https://doi.org/10.1016/j.scitotenv.2016.06.103>.
- [3] Q.X. Zhou, Y.Y. Gao, Combination of ion-pair liquid dispersive liquid-phase microextraction and high performance liquid chromatography for the determination of triazine herbicides in water samples, *Chin. Chem. Lett.* 25 (2014) 745–748, <https://doi.org/10.1016/J.CCL.2014.01.026>.
- [4] D.W. Kolpin, J.E. Barbash, R.J. Gilliom, Occurrence of pesticides in shallow groundwater of the United States: initial results from the national water-quality assessment program, *Environ. Sci. Technol.* 32 (1998) 558–566, <https://doi.org/10.1021/es970412g>.
- [5] G. Zeng, M. Chen, Z. Zeng, Risks of neonicotinoid pesticides, *Science* 340 (2013) 1403, <https://doi.org/10.1126/science.340.6139.1403-a>.
- [6] Q. Li, V.L. Snoeyink, B.J. Mariñas, C. Campos, Elucidating competitive adsorption mechanisms of ATZ and NOM using model compounds, *Water Res.* 37 (2003) 773–784, [https://doi.org/10.1016/S0043-1354\(02\)00390-1](https://doi.org/10.1016/S0043-1354(02)00390-1).
- [7] J.J. Benson, J.K. Sakkos, A. Radian, L.P. Wackett, A. Aksan, Enhanced biodegradation of ATZ by bacteria encapsulated in organically modified silica gels, *J. Colloid Interface Sci.* 510 (2018) 57–68, <https://doi.org/10.1016/j.jcis.2017.09.044>.
- [8] P. Vanraes, G. Willems, N. Daels, S.W.H.V. Hulle, K.D. Clerck, P. Surmont, F. Lynen, J. Vandamme, J.V. Durme, A. Nikiforov, C. Leys, Decomposition of ATZ traces in water by combination of non-thermal electrical discharge and adsorption on nanofiber membrane, *Water Res.* 72 (2015) 361–371, <https://doi.org/10.1016/j.watres.2014.11.009>.
- [9] J. Li, Z. Lou, B. Li, Nanostructured materials with localized surface plasmon resonance for photocatalysis, *Chin. Chem. Lett.* 33 (2022) 1154–1168, <https://doi.org/10.1016/j.cclet.2021.07.059>.
- [10] Y. Nosaka, A.Y. Nosaka, Generation and detection of reactive oxygen species in photocatalysis, *Chem. Rev.* 117 (2017) 11302–11336, <https://doi.org/10.1021/cr00161>.
- [11] S. Gligorovski, R. Strekowski, S. Barbat, D. Vione, Environmental implications of hydroxyl radicals (·OH), *Chem. Rev.* 115 (2015) 13051–13092, <https://doi.org/10.1021/cr500310b>.
- [12] P. Shandilya, S. Sambyal, R. Sharma, P. Mandyal, B. Fang, Properties, optimized morphologies, and advanced strategies for photocatalytic applications of WO₃ based photocatalysts, *J. Hazard. Mater.* (428) (2022) 128218, <https://doi.org/10.1016/j.jhazmat.2022.128218>.
- [13] H. Fan, Y. Jin, K. Liu, W. Liu, One-step MOF-templated strategy to fabrication of Ce-doped ZnIn₂S₄ tetrakaidecahedron hollow nanocages as an efficient photocatalyst for hydrogen evolution, *Adv. Sci.* 9 (2022) 2104579, <https://doi.org/10.1002/advs.202104579>.
- [14] H. Wang, L. Zhang, Z. Chen, J. Hu, S. Li, Z. Wang, J. Liu, X. Wang, Semiconductor heterojunction photocatalysts: design, construction, and photocatalytic performances, *Chem. Soc. Rev.* 43 (2014) 5234–5244, <https://doi.org/10.1039/C4CS00126E>.
- [15] W. Wang, X. Huang, S. Wu, Y. Zhou, L. Wang, H. Shi, Y. Liang, B. Zou, Preparation of p-n junction Cu₂O/BiVO₄ heterogeneous nanostructures with enhanced visible-light photocatalytic activity, *Appl. Catal. B Environ.* 134–135 (2013) 293–301, <https://doi.org/10.1016/j.apcatb.2013.01.013>.
- [16] T.M. Suzuki, S. Yoshino, K. Sekizawa, Y. Yamaguchi, A. Kudo, T. Morikawa, Photocatalytic CO₂ reduction by a Z-scheme mechanism in an aqueous suspension of particulate (CuGa)_{0.3}Zn_{1.8}S₂, BiVO₄ and a Co complex operating dual-functionally as an electron mediator and as a cocatalyst, *Appl. Catal. B Environ.* 316 (2022) 121600, <https://doi.org/10.1016/j.apcatb.2022.121600>.
- [17] J. Safaei, H. Ullah, N.A. Mohamed, M.F.M. Noh, M.F. Soh, A.A. Tahir, N.A. Ludin, M.A. Ibrahim, W.N.R.W. Isahak, M.A.M. Terid, Enhanced photoelectrochemical performance of Z-scheme g-C₃N₄/BiVO₄ photocatalyst, *Appl. Catal. B Environ.* 234 (2018) 296–310, <https://doi.org/10.1016/j.apcatb.2018.04.056>.
- [18] R. Li, F. Zhang, D. Wang, J. Yang, M. Li, J. Zhu, X. Zhou, H. Han, C. Li, Spatial separation of photogenerated electrons and holes among {010} and {110} crystal facets of BiVO₄, *Nat. Commun.* 4 (2013) 1432, <https://doi.org/10.1038/ncomms2401>.
- [19] Q. Yang, G. Tan, L. Yin, W. Liu, B. Zhang, S. Feng, Y. Bi, Y. Liu, T. Liu, Z. Wang, H. Ren, A. Xia, Full-spectrum broad-spectrum degradation of antibiotics by BiVO₄@BiOCl crystal plane S-type and Z-type heterojunctions, *Chem. Eng. J.* 467 (2023) 143450, <https://doi.org/10.1016/j.cej.2023.143450>.
- [20] J. Zhu, S. Pang, T. Dittrich, Y. Gao, W. Nie, J. Cui, R. Chen, H. An, F. Fan, C. Li, Visualizing the nano cocatalyst aligned electric fields on single photocatalyst particles, *Nano Lett.* 17 (2020) 6735–6741, <https://doi.org/10.1021/acs.nanolett.7b02799>.
- [21] B.M. Bresolin, C. Günemann, D.W. Bahnemann, M. Sillanpää, Pb-Free Cs₃Bi₂I₉ perovskite as a visible-light-active photocatalyst for organic pollutant degradation, *Nanomaterials* 10 (2020) 763, <https://doi.org/10.3390/nano10040763>.
- [22] Z. Liu, R. Liu, Y. Mu, Y. Feng, G. Dong, M. Zhang, T. Lu, In situ construction of lead-free perovskite direct Z-scheme heterojunction Cs₃Bi₂I₉/Bi₂WO₆ for efficient photocatalysis of CO₂ reduction, *Sol. RRL* 5 (2021) 2000691, <https://doi.org/10.1002/solr.202000691>.
- [23] R. Waykar, A. Bhorde, S. Nair, S. Pandharkar, B. Gabhale, R. Aher, S. Rondiya, A. Waghmare, V. Doiphode, A. Punde, P. Vairale, M. Prasad, S. Jadkar, Environmentally stable lead-free cesium bismuth iodide (Cs₃Bi₂I₉) perovskite: synthesis to solar cell application, *J. Phys. Chem. Solids* 146 (2020) 109608, <https://doi.org/10.1016/j.jpcs.2020.109608>.
- [24] S. Song, Z. Xing, H. Zhao, Z. Li, W. Zhou, Recent advances in bismuth-based photocatalysts: environment and energy applications, *Green. Energy Environ.* 8 (2023) 1232–1264, <https://doi.org/10.1016/j.gee.2022.04.004>.
- [25] D. Kumar, J. Kaur, P.P. Mohanty, R. Ahuja, S. Chakraborty, Recent advancements in nontoxic halide perovskites beyond divalent composition space, *ACS Omega* 6 (2021) 33240–33252, <https://doi.org/10.1021/acsomega.1c05333>.
- [26] H. Xu, Y. Ma, J. Chen, W. Zhang, J. Yang, Electrocatalytic reduction of nitrate - a step towards a sustainable nitrogen cycle, *Chem. Soc. Rev.* 51 (2022) 2710–2758, <https://doi.org/10.1039/D1CS00857A>.
- [27] Q. Li, Y. Liu, Z. Wan, H. Cao, S. Zhang, Y. Zhou, X. Ye, X. Liu, D. Zhang, Microwave-assisted synthesis of oxygen vacancy associated TiO₂ for efficient photocatalytic nitrate reduction, *Chin. Chem. Lett.* 33 (2023) 3835–3841, <https://doi.org/10.1016/j.cclet.2021.12.025>.
- [28] X. Li, M. Zhang, J. Feng, C. Bai, Y. Ren, Electrostatic self-assembly to form unique LiNbO₃/ZnS core-shell structure for photocatalytic nitrate reduction enhancement, *J. Colloid Interface Sci.* 607 (2022) 1323–1332, <https://doi.org/10.1016/j.jcis.2021.09.069>.
- [29] H.O.'N. Tugaoen, S. Garcia-Segura, K. Hristovski, P. Westerhoff, Challenges in photocatalytic reduction of nitrate as a water treatment technology, *Sci. Total Environ.* 599–600 (2017) 1524–1551, <https://doi.org/10.1016/j.scitotenv.2017.04.238>.
- [30] I. Katz, M. Green, Y. Ruskof, C.G. Dosoretz, Characterization of ATZ degradation and nitrate reduction by *Pseudomonas* sp. strain ADP, *Adv. Environ. Res.* 4 (2000) 211–218, [https://doi.org/10.1016/S1093-0191\(00\)00022-8](https://doi.org/10.1016/S1093-0191(00)00022-8).
- [31] B. Tepuš, M. Simonić, I. Petrić, Comparison between nitrate and pesticide removal from ground water using adsorbents and NF and RO membranes, *J. Hazard. Mater.* 170 (2009) 1210–1217, <https://doi.org/10.1016/j.jhazmat.2009.05.105>.

- [32] R.F. Spalding, M.E. Exner, D.D. Snow, D.A. Cassada, M.E. Burbach, S.J. Monson, Herbicides in ground water beneath Nebraska's management systems evaluation area, *J. Environ. Qual.* 32 (2003) 92–99, <https://doi.org/10.2134/jeq2003.9200>.
- [33] L.T. Stayner, K. Almberg, R. Jones, J. Gruber, M. Pedersen, M. Turyk, ATZ and nitrate in drinking water and the risk of preterm delivery and low birth weight in four Midwestern states, *Environ. Res.* 152 (2017) 294–303, <https://doi.org/10.1016/j.envres.2016.10.022>.
- [34] P. Calza, D. Vione, A. Novelli, E. Pelizzetti, C. Minero, The role of nitrite and nitrate ions as photosensitizers in the phototransformation of phenolic compounds in seawater, *Sci. Total Environ.* 439 (2012) 67–75, <https://doi.org/10.1016/j.scitotenv.2012.09.009>.
- [35] S. Zhou, L. Li, Y. Wu, S. Zhu, N. Zhu, L. Bu, D.D. Dionysiou, UV₃₆₅ induced elimination of contaminants of emerging concern in the presence of residual nitrite: roles of reactive nitrogen species, *Water Res.* 178 (2020) 115829, <https://doi.org/10.1016/j.watres.2020.115829>.
- [36] D.-H. Kim, J. Lee, J. Ryu, K. Kim, W. Choi, Arsenite oxidation initiated by the UV photolysis of nitrite and nitrate, *Environ. Sci. Technol.* 48 (2014) 4030–4037, <https://doi.org/10.1021/es500001q>.
- [37] R.C. Scholes, C. Prasse, D.L. Sedlak, The role of reactive nitrogen species in sensitized photolysis of wastewater-derived trace organic contaminants, *Environ. Sci. Technol.* 53 (2019) 116483–116491, <https://doi.org/10.1021/acs.est.9b01386>.
- [38] D. Vione, V. Maurino, C. Minero, M. Vincenti, E. Pelizzetti, Formation of nitrophenols upon UV irradiation of phenol and nitrate in aqueous solutions and in TiO₂ aqueous suspensions, *Chemosphere* 44 (2001) 237–248, [https://doi.org/10.1016/S0045-6535\(00\)00170-3](https://doi.org/10.1016/S0045-6535(00)00170-3).
- [39] L. Ge, J. Chen, X. Qiao, J. Lin, X. Cai, Light-source-dependent effects of main water constituents on photodegradation of penicilin antibiotics: mechanism and kinetics, *Environ. Sci. Technol.* 43 (2009) 3101–3107, <https://doi.org/10.1021/es8031727>.
- [40] C. Hou, X. Jiang, D. Chen, X. Zhang, X. Liu, Y. Mu, J. Shen, Ag-TiO₂/biofilm/nitrate interface enhanced visible light-assisted biodegradation of tetracycline: the key role of nitrate as the electron acceptor, *Water Res.* 215 (2022) 118212, <https://doi.org/10.1016/j.watres.2022.118212>.
- [41] Y. Huang, M. Kong, D. Westerman, E.G. Xu, S. Coffin, K.H. Cochran, Y. Liu, S. D. Richardson, D. Schlenk, D.D. Dionysiou, Effects of HCO₃⁻ on degradation of toxic contaminants of emerging concern by UV/NO₃⁻, *Environ. Sci. Technol.* 52 (2018) 12697–12707, <https://doi.org/10.1021/acs.est.8b04383>.
- [42] F. Xing, R. Zeng, C. Cheng, Q. Liu, C. Huang, POM-incorporated ZnIn₂S₄ Z-scheme dual-functional photocatalysts for cooperative benzyl alcohol oxidation and H₂ evolution in aqueous solution, *Appl. Catal. B Environ.* 306 (2022) 121087, <https://doi.org/10.1016/j.apcatb.2022.121087>.
- [43] N. Gregory, Carbon tetrachloride toxicity and electron capture, *Nature* 212 (1966) 1460–1461, <https://doi.org/10.1038/2121460a0>.
- [44] C. Minero, V. Maurino, E. Pelizzetti, D. Vione, Assessing the steady-state [·NO₂] in environmental samples, *Environ. Sci. Pollut. Res.* 14 (2007) 241–243, <https://doi.org/10.1065/espr2007.01.382>.
- [45] Y. Yuan, L. Feng, X. He, M. Wu, Z. Ai, L. Zhang, J. Gong, Nitrate promoted defluorination of perfluoroctanoic acid in UV/sulfite system: coupling hydrated electron/reactive nitrogen species-mediated reduction and oxidation, *Environ. Pollut.* 313 (2022) 120172, <https://doi.org/10.1016/j.enpol.2022.120172>.
- [46] T. Lu, F. Chen, Multiwfns: a multifunctional wavefunction analyzer, *J. Comput. Chem.* 33 (2012) 580–592, <https://doi.org/10.1002/jcc.22885>.
- [47] T. Lu, Q. Chen, Realization of conceptual density functional theory and information-theoretic approach in Multiwfns program, in: Conceptual Density Functional Theory, WILEY-VCH GmbH, Weinheim, 2022, pp 631–647. (<https://doi.org/10.1002/9783527829941.ch31>).
- [48] W. Humphrey, A. Dalke, K. Schulten, VMD: visual molecular dynamics, *J. Mol. Graph.* 14 (1996) 33–38, [https://doi.org/10.1016/0263-7855\(96\)00018-5](https://doi.org/10.1016/0263-7855(96)00018-5).
- [49] M. Ou, S. Wan, Q. Zhong, S. Zhang, Y. Song, L. Guo, W. Cai, Y. Xu, Hierarchical Z-scheme photocatalyst of g-C₃N₄@Ag/BiVO₄ (040) with enhanced visible-light-induced photocatalytic oxidation performance, *Appl. Catal. B Environ.* 221 (2018) 97–107, <https://doi.org/10.1016/j.apcatb.2017.09.005>.
- [50] S. Chen, D. Huang, G. Zeng, W. Xue, L. Lei, P. Xu, R. Deng, J. Li, M. Cheng, In-situ synthesis of facet-dependent BiVO₄/Ag₃PO₄/PANI photocatalyst with enhanced visible-light-induced photocatalytic degradation performance: synergism of interfacial coupling and hole-transfer, 122840–122840, *Chem. Eng. J.* 382 (2020), <https://doi.org/10.1016/j.cej.2019.122840>.
- [51] R. Li, H. Han, F. Zhang, D. Wang, C. Li, Highly efficient photocatalysts constructed by rational assembly of dual-cocatalysts separately on different facets of BiVO₄, *Energy Environ. Sci.* 7 (2014) 1369–1376, <https://doi.org/10.1039/C3EE43304H>.
- [52] Q. Yang, G. Tan, B. Zhang, S. Feng, Y. Bi, Z. Wang, A. Xia, H. Ren, W. Liu, Cs_{0.35}WO₃(t-m)-BiVO₄ double Z-type heterojunction photothermal synergistic enhanced full-spectrum degradation of antibiotics, *Chem. Eng. J.* 458 (2023) 141378, <https://doi.org/10.1016/j.cej.2023.141378>.
- [53] C. Cheng, J. Fang, S. Lu, C. Cen, Y. Chen, L. Ren, W. Feng, Z. Fang, Zirconium metal-organic framework supported highly-dispersed nanosized BiVO₄ for enhanced visible-light photocatalytic applications, *J. Chem. Technol. Biotechnol.* 91 (2016) 2785–2792, <https://doi.org/10.1002/jctb.4885>.
- [54] D. Majhi, K. Das, A. Mishra, R. Dhiman, B.G. Mishra, One pot synthesis of CdS/BiOBr/Bi₂O₃CO₃: a novel ternary double Z-scheme heterostructure photocatalyst for efficient degradation of atrazine, *Appl. Catal. B Environ.* 260 (2020) 118222, <https://doi.org/10.1016/j.apcatb.2019.118222>.
- [55] S. Wang, Y. Wang, J. Wan, Y. Ma, Z. Yan, G. Zhang, Dual channel carrier transfer based on Ti₃C₂Tx improves carrier utilization of Z-scheme Ag₃PO₄/AgBr heterojunction photocatalyst, *Sep. Purif. Technol.* 253 (2020) 117486, <https://doi.org/10.1016/j.seppur.2020.117486>.
- [56] X. Chen, J. Wang, Y. Chai, Z. Zhang, Y. Zhu, Efficient photocatalytic overall water splitting induced by a giant internal electric field of g-C₃N₄/rGO/PDIP Z-scheme heterojunction, *Adv. Mater.* 33 (2021) 2007479, <https://doi.org/10.1002/adma.202007479>.
- [57] T. Kanata-Kito, M. Matsunaga, H. Takakura, Y. Hamakawa, T. Nishino, Photoreflectance characterization of built-in potential in MBE-produced As-grown GaAs surface, *Proc. SPIE* 1286 (1990) 56–65, <https://doi.org/10.1117/12.20837>.
- [58] J. Zhao, N. Li, R. Yu, Z. Zhao, J. Nan, Magnetic field enhanced denitrification in nitrate and ammonia contaminated water under 3D/2D Mn₂O₃/g-C₃N₄ photocatalysis, *Chem. Eng. J.* 349 (2018) 530–538, <https://doi.org/10.1016/j.cej.2018.05.124>.
- [59] Y. Xue, P. Wang, C. Wang, Y. Ao, Efficient degradation of atrazine by BiOBr/UiO-66 composite photocatalyst under visible light irradiation: environmental factors, mechanisms and degradation pathways, *Chemosphere* 203 (2018), <https://doi.org/10.1016/j.chemosphere.2018.04.017>.
- [60] J.M.D. Dikdim, Y. Gong, G.B. Noumi, J.M. Sielechi, X. Zhao, N. Ma, M. Yang, J. B. Tchatchueng, Peroxymonosulfate improved photocatalytic degradation of atrazine by activated carbon/graphitic carbon nitride composite under visible light irradiation, *Chemosphere* 217 (2019) 833–842, <https://doi.org/10.1016/j.chemosphere.2018.10.177>.
- [61] W.-K. Jo, N.C.S. Selvam, Z-scheme CdS/g-C₃N₄ composites with RGO as an electron mediator for efficient photocatalytic H₂ production and pollutant degradation, *Chem. Eng. J.* 317 (2017) 913–924, <https://doi.org/10.1016/j.cej.2017.02.129>.
- [62] Y. Zhang, C. Han, M.N. Nadagouda, D.D. Dionysiou, The fabrication of innovative single crystal N,F-codoped titanium dioxide nanowires with enhanced photocatalytic activity for degradation of atrazine, *Appl. Catal. B Environ.* 168–169 (2015) 550–558, <https://doi.org/10.1016/j.apcatb.2015.01.009>.
- [63] C. Yang, Z. Zhang, P. Wang, P. Xu, T. Shen, Y. Xin, G. Zhang, A novel vertical immobilized photocatalytic membrane reactor based on Bi₂WO₆-g-C₃N₄/PVDF for enhanced removal of atrazine, anti-fouling performance and long-term stability, *Chem. Eng. J.* 471 (2023) 144672, <https://doi.org/10.1016/j.cej.2023.144672>.
- [64] K. Wei, A. Armutulu, Y. Wang, G. Yao, R. Xie, B. Lai, Visible-light-driven removal of atrazine by durable hollow core-shell TiO₂@LaFeO₃ heterojunction coupling with peroxymonosulfate via enhanced electron-transfer, *Appl. Catal. B Environ.* 303 (2022) 120889, <https://doi.org/10.1016/j.apcatb.2021.120889>.
- [65] R. Akbarzadeh, Q. Ibrahim and T.-C. Jen, "Photocatalysis and energy cost analysis of vanadia titania thin films synthesis," 2019 International Conference on Power Generation Systems and Renewable Energy Technologies (PGSRET), Istanbul, Turkey, 2019, pp. 1–3, <https://doi.org/10.1109/PGSRET.2019.8882666>.
- [66] L. Khatua, R. Panda, A.K. Nayak, A. Singh, P.K. Sahoo, D. Pradhan, U.P. Singh, S. K. Das, Efficient UV photocatalytic dye decomposition activity with cost effective solid state reaction grown Zinc Orthotitanate (Zn₂TiO₄) nanoparticles, *J. Alloy. Compd.* 764 (2018) 895–900, <https://doi.org/10.1016/j.jallcom.2018.06.126>.
- [67] N. Hashim, S. Thakur, M. Patang, F. Crapulli, A.K. Ray, Solar degradation of diclofenac using Eosin-Y-activated TiO₂: cost estimation, process optimization and parameter interaction study, *Environ. Technol. Chem.* 38 (2017) 933–944, <https://doi.org/10.1080/09593330.2016.1214625>.
- [68] M.G. Alalm, A. Tawfik, S. Ookawara, Solar photocatalytic degradation of phenol by TiO₂/AC prepared by temperature impregnation method, *Desalin. Water Treat.* 57 (2014) 835–844, <https://doi.org/10.1080/19443994.2014.969319>.
- [69] S. Goldstein, A. Russo, A. Samuni, Reactions of PTIO and Carboxy-PTIO with -NO, -NO₂, and O₂⁻, *J. Biol. Chem.* 278 (2003) 50949–50955, <https://doi.org/10.1074/jbc.M308317200>.
- [70] H. Chen, T. Lin, P. Wang, Y. Wang, W. Wei, S. Zhu, A novel solar-activated chlorine dioxide process for ATZ degradation in drinking water, *Water Res.* 239 (2023) 120056, <https://doi.org/10.1016/j.watres.2023.120056>.
- [71] J.A. Khan, X. He, N.S. Shah, M. Sayed, H.M. Khan, D.D. Dionysiou, Degradation kinetics and mechanism of desethyl-atrazine and desisopropyl-atrazine in water with -OH and SO₄²⁻ based-AOPs, *Chem. Eng. J.* 325 (2017) 485–494, <https://doi.org/10.1016/j.cej.2017.05.011>.
- [72] L. Bu, N. Zhu, C. Li, Y. Huang, M. Kong, X. Duan, D.D. Dionysiou, Susceptibility of ATZ photo-degradation in the presence of nitrate: Impact of wavelengths and significant role of reactive nitrogen species, *J. Hazard. Mater.* 388 (2020) 121760, <https://doi.org/10.1016/j.jhazmat.2019.121760>.
- [73] J. Li, J. Zou, S. Zhang, H. Cai, Y. Huang, J. Lin, Q. Li, B. Yuan, J. Ma, Sodium tetraborate simultaneously enhances the degradation of acetaminophen and reduces the formation potential of chlorinated by-products with heat-activated peroxymonosulfate oxidation, *Water Res.* 224 (2022) 119095, <https://doi.org/10.1016/j.watres.2022.119095>.